RESEARCH ARTICLE

Correspondence to:
T. Miles,
tnmiles@marine.rutgers.edu

Coastal ocean circulation during Hurricane Sandy

Travis Miles[1] (ID)**, Greg Seroka[2]** (ID)**, and Scott Glenn[1]**

[1]Department of Marine and Coastal Sciences, Rutgers University Center for Ocean Observing Leadership, New Brunswick, New Jersey, USA, [2]Ocean Prediction Center, NOAA/NWS/NCEP, College Park, Maryland, USA

Abstract Hurricane Sandy (2012) was the second costliest tropical cyclone to impact the United States and resulted in numerous lives lost due to its high winds and catastrophic storm surges. Despite its impacts little research has been performed on the circulation on the continental shelf as Sandy made landfall. In this study, integrated ocean observing assets and regional ocean modeling were used to investigate the coastal ocean response to Sandy's large wind field. Sandy's unique cross-shelf storm track, large size, and slow speed resulted in along-shelf wind stress over the coastal ocean for nearly 48 h before the eye made landfall in southern New Jersey. Over the first inertial period (∼18 h), this along-shelf wind stress drove onshore flow in the surface of the stratified continental shelf and initiated a two-layer downwelling circulation. During the remaining storm forcing period a bottom Ekman layer developed and the bottom Cold Pool was rapidly advected offshore ∼70 km. This offshore advection removed the bottom Cold Pool from the majority of the shallow continental shelf and limited ahead-of-eye-center sea surface temperature (SST) cooling, which has been observed in previous storms on the MAB such as Hurricane Irene (2011). This cross-shelf advective process has not been observed previously on continental shelves during tropical cyclones and highlights the need for combined ocean observing systems and regional modeling in order to further understand the range of coastal ocean responses to tropical cyclones.

Plain Language Summary Hurricane Sandy (2012) was the second costliest tropical cyclone to impact the United States and resulted in numerous lives lost due to its high winds and catastrophic storm surges. Despite its impacts little research has been performed on the circulation of the coastal ocean as Sandy made landfall. In this study integrated ocean observing assets and regional ocean modeling were used to investigate the coastal ocean response to Sandy's large wind field. Sandy's unique cross-shelf storm track, large size, and slow speed resulted in powerful alongshore winds over the coastal ocean for nearly 48 h before the eye made landfall in southern New Jersey. These winds transported cold bottom waters offshore and left the coastal ocean uniformly warm and mixed. This circulation pattern has not been observed previously during tropical cyclones and highlights the need for a continued focus on coastal ocean observing systems and numerical modeling during storm events.

1. Introduction

Tropical cyclones (TCs) are among the deadliest and costliest natural hazards on earth. In the US alone they are responsible for nearly half of all billion dollar natural disasters, and account for over 3000 deaths between 1980 and 2016 (https://www.ncdc.noaa.gov/billions/). Globally, individual storms can be extremely deadly such as Nargis, which lead to over 100,000 fatalities in Myanmar in 2008 [*Fritz et al.*, 2009]. TC track forecasts have improved dramatically since 1970, yet similar dramatic progress has not been made in TC intensity prediction [*DeMaria et al.*, 2014; *Cangialosi and Franklin*, 2016]. Predictions of TC rapid intensification or deintensification just before landfall remain a critical challenge within this intensity gap. Rapid intensification in the hours before landfall has the potential to catch coastal communities off guard, while unexpected rapid deintensification may erode future forecast credibility among the public [*Considine et al.*, 2004]. Uncertain modeling of the ocean response to and feedback on TCs remains a critical factor that has limited improvement in intensity forecasts [*Emanuel et al.*, 2004; *Yablonsky and Ginis*, 2009; *Emanuel*, 2016], particularly in the coastal ocean just prior to landfall [*Glenn et al.*, 2016; *Seroka et al.*, 2016]. This manuscript contributes to a growing body of work that details the response of the coastal ocean to TCs. Specifically, this work focuses on the stratified coastal ocean response ahead of and during Hurricane Sandy, the second

costliest storm to impact the US ($\sim$\$68 billion USD in damages and 159 lives lost https://www.ncdc.noaa.gov/billions/).

Small changes in sea surface temperature (SST)—$\sim$1°C—can impact TC intensity [*Price*, 1981; *Emanuel*, 1999; *Bender and Ginis*, 2000; *Emanuel et al.*, 2004; *Yablonsky and Ginis*, 2008], as the ocean provides a source of heat for atmospheric convection [*Black et al.*, 2007; *Jaimes and Shay*, 2015]. In the deep ocean, TCs have been found to drive upwelling and mixing of cold nutrient rich water to the sea surface since the mid 1900s [*Hidaka and Akiba*, 1955; *Fisher*, 1958; *Leipper*, 1967]. These events, frequently referred to as "cold wakes," are typically observable by satellite [*Stramma et al.*, 1986; *Cornillon et al.*, 1987] and can produce large phytoplankton blooms in the days following storm passage [*Wang and Zhao*, 2008]. Focused field campaigns such as the Coupled Boundary Layer Air-Sea Transfer Experiment (CBLAST) have used a combination of atmosphere and ocean observations and modeling to show that storm-driven mixing over the deep ocean can reduce heat transfer to the atmosphere [*Black et al.*, 2007; *Chen et al.*, 2007]. Extensive literature exists detailing both the deep ocean response to TCs as well as storm surge impacts, yet comparatively little work has been done over continental shelves. One of these few studies has indicated that in some coastal regions rapid intensification is expected to increase as the planet warms [*Emanuel*, 2016]. Others have focused on TCs entering midlatitudes, and have shown that rapid deintensification occurs when storms cross the highly stratified continental shelves [*Glenn et al.*, 2016]. Existing operational coupled atmosphere-ocean TC models have failed to accurately capture the ocean response that leads to this rapid deintensification.

The source of the cold water on the Mid Atlantic (MAB) Bight shelf, which can be mixed to the surface and lead to rapid storm deintensification [*Glenn et al.*, 2016; *Seroka et al.*, 2016], is a seasonal feature known as the summer Cold Pool [*Houghton et al.*, 1982]. The Cold Pool is a near bottom water mass that extends from the southern edge of Georges Bank along the MAB continental midshelf and outer-shelf to Cape Hatteras, NC. The Cold Pool is formed in the spring as thermal heating develops a seasonal thermocline over cold remnant winter water. This thermocline reaches its peak strength in July and August when surface to bottom temperature differences can exceed 15°C and the surface mixed layer is typically between 10 and 20 m thick across the shelf [*Castelao et al.*, 2008]. This stratification begins to break down in September through a combination of reduced solar heating, falling atmospheric temperatures, and most notably fall transition storms, which periodically vertically mix the water column [*Houghton et al.*, 1982; *Lentz*, 2003, 2017; *Glenn et al.*, 2008].

Hurricane Irene in 2011 was a relatively heavily sampled storm that impacted the MAB continental shelf and serves as an ideal case study of rapid deintensification. Irene made landfall in New Jersey in late August of 2011 [*Avila and Cangialosi*, 2012] when MAB stratification was near its peak. A study by *Glenn et al.* [2016] showed that onshore winds forced the surface mixed layer toward the NJ coastline setting up an offshore-directed pressure gradient that forced an offshore bottom layer flow, enhancing vertical shear and mixing over the midshelves and outer-shelves where stratification was greatest. SSTs were reduced ahead-of-eye-center by over $\sim$4.5°C at a coastal buoy, accounting for 82% of the total storm cooling at that location. This study showed that out of the 11 storms that have traversed the MAB between 1985 and 2016 during the summer stratified season, 73% of the overall cooling across all storms at selected coastal buoy locations occurred ahead-of-eye-center with an average cooling of 2.7°C. In Irene, this cooling represented the largest factor contributing to the storm's deintensification just prior to its NJ landfall—not track, wind shear, or dry air intrusion [*Seroka et al.*, 2016].

Hurricane Sandy made landfall in New Jersey 14 months after Irene in nearly the same location [*Blake et al.*, 2013]. Despite its catastrophic damages, Hurricane Sandy also weakened and was designated as posttropical as it crossed the continental shelf of the MAB. Unlike Irene, MAB SSTs during Sandy were only reduced by $\sim$2°C. Coupled ocean-atmosphere model hindcasts [*Zambon et al.*, 2014] showed Sandy's weakening was linked to large-scale synoptic atmospheric circulation and was insensitive to air-sea coupling. This study hypothesized that the MAB had already undergone its fall transition, limiting the impact of the MAB ocean on atmospheric processes. Yet, observations from an autonomous underwater glider deployed ahead of Sandy showed the Cold Pool and stratification was still present on the MAB shelf, although to a lesser degree than in Irene [*Miles et al.*, 2015]. The dichotomy between the ocean's impact on the intensities of Irene and Sandy indicates that more focused studies of the stratified coastal ocean response to a wide range of landfalling TCs are critical. In this manuscript, we investigate the coastal ocean response of the

Cold Pool to Sandy's powerful and long-lasting winds as the storm crossed the MAB continental shelf. We use a unique data set from a Teledyne Webb Slocum autonomous underwater glider and process-focused numerical simulations with the Regional Ocean Modeling System (ROMS). Understanding these processes will be critical to improving and building confidence in short-term forecasts of storm intensity as storms cross continental shelves and approach increasingly vulnerable population centers [*Miller et al.*, 2009; *Kossin et al.*, 2014].

2. Methods

Ocean observing systems have developed into critical networks of instruments capable of sampling the coastal ocean in three dimensions before, during, and after storm events [*Kohut et al.*, 2006; *Miles et al.*, 2013, 2015; *Domingues et al.*, 2015; *Glenn et al.*, 2016]. Hurricane Sandy made landfall after crossing through the Mid Atlantic Regional Association Coastal Ocean Observing System (MARACOOS), a certified Regional Information Coordination Entity (RICE) of the U.S. Integrated Ocean Observing System (IOOS) [*Briscoe et al.*, 2008]. These systems typically include a range of technologies such as satellite observations, high frequency (HF) Radars, met-ocean buoys, autonomous underwater gliders, among many others and support regional ocean data products and forecasts through data assimilation and model validation. Technologies used in this study and described below include autonomous underwater gliders, HF Radar, and numerical model technologies that were developed and supported through MARACOOS over the past decade.

2.1. Gliders

Autonomous underwater gliders have become reliable technologies for sampling the ocean in extreme weather conditions [*Glenn et al.*, 2008, 2016; *Ruiz et al.*, 2012; *Miles et al.*, 2013, 2015; *Domingues et al.*, 2015; *Swart et al.*, 2015; *Nicholson et al.*, 2016; *du Plessis et al.*, 2017]. The ability of Teledyne Webb Research manufactured Slocum gliders to access shallow (<100 m) continental shelves and their modular science bay design make them uniquely suited for rapid deployment to sample coastal storm events. Slocum gliders move vertically through the water column by using a pump in the fore section to change volume and shifting ballast to alter pitch to dive and climb at $\sim$15–20 cm s^{-1}. The glider body shape, wings, and nominal pitch angle of $\pm$26.5° result in forward motion of $\sim$20 km d^{-1} relative to the moving water column. Integrated sensors typically collect data at 0.5 Hz and send data back to shore in near real-time through an Iridium Satellite cellphone in the tail section. Rutgers University glider RU23 data were used in this study to investigate the evolution of the thermal structure and water column velocities on the continental shelf during Hurricane Sandy storm conditions. Previously these data were also used to investigate sediment resuspension and transport in Sandy by *Miles et al.* [2015]. RU23 was programmed to surface at 2 h intervals in order to provide high temporal resolution data during the storm. This glider was equipped with an unpumped Seabird glider conductivity, temperature, and depth (CTD) sensor; two Wetlabs, Inc. Eco Triplets with two channels measuring chlorophyll fluorescence, colored dissolved organic matter, and four channels of optical backscatter; and an externally mounted internally logging 2 MHz transducer Nortek Aquadopp current profiler.

Thermal inertia of the conductivity cell has remained a challenge for calculating high-quality salinity and density parameters with unpumped glider CTDs in regions with large temperature gradients such as those found on the MAB. Attempts at thermal lag correction to conductivity and subsequent salinity and density calculations following the *Garau et al.* [2011] minimization technique were unsuccessful. This is likely due to the exceptionally large thermal stratification, which exceeds what was successfully tested in that study, as well as the difficulty in finding consistent time offsets with the unpumped glider CTD. To address this issue, we calculate density by removing salinity data after large temperature changes in each profile (e.g., below the thermocline on glider dives and above the thermocline on the subsequent climb) and utilize the nearest-bottom salinity on dives and nearest-surface salinity on climbs to represent that layer's salinity for density calculations. While crude, this approach maintains water column stability. Further, the MAB density structure is dominated by temperature rather than salinity, so there is a limited impact on final density calculations. Temperature and corrected salinity and density fields were binned into 2 m bins. With the glider fall velocity of $\sim$15–20 cm s^{-1} and CTD sample rate at 0.5 Hz this resulted in over 10 points per bin. These binned data were used to estimate buoyancy frequency as:

$$N^2 = \frac{g}{\rho_o} \frac{\partial \sigma_\theta}{\partial z} \tag{1}$$

where N is the buoyancy frequency, g is gravity, ρ_o is a reference density of 1025 kg m^{-3}, σ_θ is potential density anomaly, and z is depth.

The Nortek Aquadopp current profiler was an externally mounted and independently logging three-beam 2 MHz instrument. It was mounted in an upward looking orientation for practical deployment and recovery purposes and to not block downward looking optical sensors. The transducer head was custom made to be oriented vertically at a glider pitch angle of 26.5°. Data collection was configured with 10 1 m bins and a 0.2 m blanking distance, and samples in beam coordinates were collected at 1 Hz. To rotate beam coordinates into east, north, and up (ENU) pitch and roll were used from the Nortek Aquadopps internal sensor, while heading information after timestamp alignment was interpolated from the glider compass. This was done to minimize magnetic interference from the moving battery pack and pump system in the fore section of the glider, which was closer to the mounting location of the Aquadopp than the aft mounted glider compass. To estimate realistic water column velocities a method typically used for lowered acoustic Doppler current profilers [*Visbeck*, 2002], and which has been adapted for use on Spray [*Todd et al.*, 2011a, 2011b] and Slocum [*Miles et al.*, 2015] gliders was used. This method uses the Aquadopp to determine water column vertical shear during a glider segment (glider dive and surfacing) and constrains these shear velocities with the glider dead-reckoned depth averaged current [*Davis et al.*, 2002] to determine the absolute water column velocity. The time resolution of these currents is dependent on the length of time between each glider surfacing, which can vary. In this case, the glider surfaced approximately every 2 h as stated above in an effort to resolve tidal variability as well as the rapidly changing currents induced by Sandy.

2.2. HF Radar
The MAB has one of the largest continuous networks of CODAR HF Radar stations globally, ranging from North Carolina to Massachusetts. HF Radar uses the Doppler shift of backscattered radio frequencies from surface waves to measure the radial component of ocean surface currents, i.e. toward or away from each station [*Barrick*, 1971a,1971b; *Teague*, 1971]. Radial data are collected continuously and overlapping radials are combined via an optimal interpolation method to produce hourly total surface current maps hourly [e.g., *Kohut et al.*, 2012]. The network in the MAB, managed through MARACOOS, consists of nested 5, 13, and 25 MHz networks [*Roarty et al.*, 2010]. The 5 MHz network used in this study is capable of measuring surface currents out to the shelf-break, approximately 150 km offshore in ideal wave conditions and has a nominal spatial resolution of 6 km. The MARACOOS HF Radar network was operating at full capacity during Sandy's approach, but storm surges destroyed numerous stations reducing data coverage and quality starting at 3:00 GMT on 31 October 2012.

2.3. Atmospheric Model
The atmospheric model used in this study was the RUCOOL implementation of the Weather Research and Forecasting Advanced Research WRF (WRF-ARW) model developed at NCAR [*Skamarock et al.*, 2008]. The forcing was previously used in *Miles et al.* [2015] and is configured with 6 km horizontal resolution, 35 vertical levels, horizontal boundary conditions from the Global Forecasting System (GFS) 0.5° operational configuration at the time, and a coldest-pixel composite SST bottom boundary condition from the Advanced Very High Resolution Radiometer (AVHRR) and NASA SPoRT [*Glenn et al.*, 2016]. The SST bottom boundary condition is held static within each 36 h hindcast cycle, since there were very few new datapoints to add to each composite interval due to Sandy's extensive cloud cover. This static bottom boundary is appropriate based on the limited impact of air-sea coupling affecting Sandy's wind field [*Zambon et al.*, 2014]. This WRF product is similar to the one used in previous studies [*Georgas et al.*, 2014; *Glenn et al.*, 2016; *Seroka*, 2016] and covers the entire MAB (Figure 1). Data were output hourly from a series of six 36 h forecast runs reinitialized at 00:00 GMT daily starting on 25 October. We combined hourly output from hour 7 to 30 and removed hours 0 to 6 to minimize the impact of model spin-up time on the final continuous hourly forcing. Please see *Miles et al.* [2015] for further details of the WRF atmospheric model configuration used in this study.

The WRF model output used in this study was previously compared with buoys 44009 and 44025 in *Miles et al.* [2015]. This comparison showed that simulated winds and pressure compared qualitatively well with
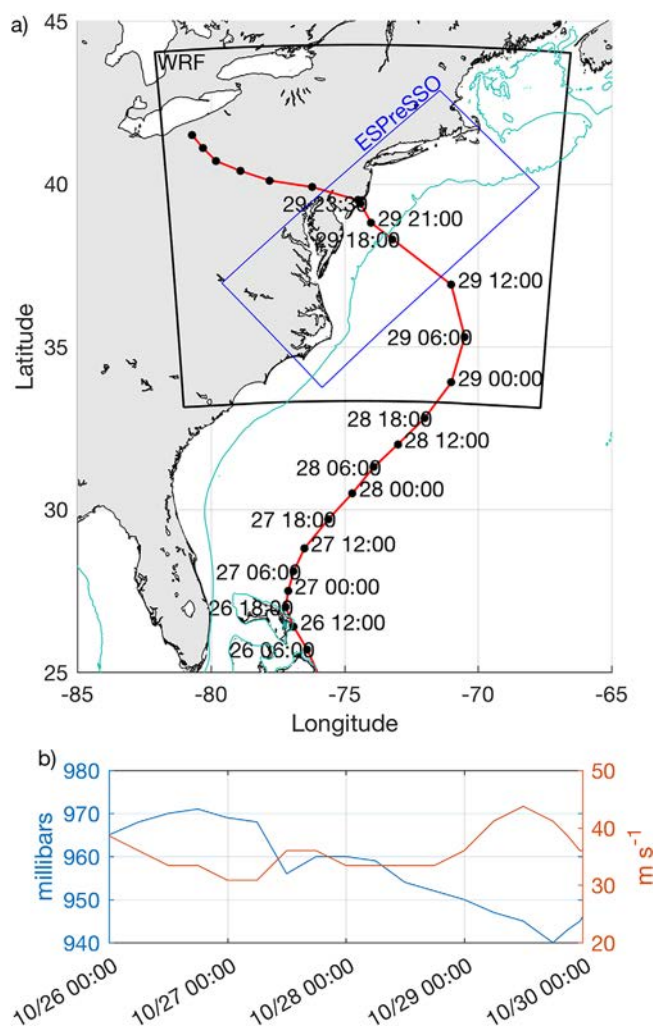
Figure 1. A map (a) of the WRF model domain (black box), ROMS ESPreSSO model domain (blue box), NHC best track positions (red line) and times (dd HH:MM in black), and the 100 m isobath (teal line). A time series (b) of the NHC best track pressure (blue) and maximum wind speed (orange).

observations and had correlation coefficients of 0.87 and 0.90 with winds at 44009 and 44025, respectively, and 0.99 with pressure at both buoys. Sandy track comparisons between modeled minimum pressure and the NHC best track estimates as the eye transited across the continental shelf (Figure 2) show the modeled track staying slightly north of the NHC best track until the final hour before landfall. The maximum separation between the two tracks during this time period is less than 35 km and was less than 10 km at landfall, well within the NHC best track estimate uncertainties of 80 to 30 km for tropical depressions and category 4 to 5 hurricanes, respectively, in the Atlantic Basin [*Torn and Snyder*, 2012].

2.4. Hydrodynamic Model

We performed numerical model simulations of the coastal ocean response to Sandy using the Regional Ocean Modeling System (ROMS) [*Shchepetkin and McWilliams*, 2005, 2009a, 2009b; *Haidvogel et al.*, 2008] with the Experimental System for Predicting Shelf and Slope Optics (ESPreSSO) domain [*Cahill et al.*, 2008; *Haidvogel et al.*, 2008; *Hofmann et al.*, 2008; *Zhang et al.*, 2009; *Xu et al.*, 2013]. ROMS is a free surface, sigma-coordinate, primitive equation numerical ocean model that has been used extensively to investigate regional ocean processes globally. The ESPreSSO domain (Figure 1) includes the entire MAB from within bays out past the shelf-break with 5 km horizontal resolution and 36 vertical levels. ESPreSSO uses

Four-dimensional variational (4D-Var) data assimilation to obtain the best state estimate of the coastal ocean in near real-time [*Moore et al.*, 2011] and has been running nearly continuously since 2006. The standard ESPreSSO configuration uses boundary conditions from the Hybrid Coordinate Ocean Model (HYCOM) Navy Coupled Ocean Data Assimilation (NCODA) forecast system (http://hycom.org/), tides from the Advanced CIRCulation (ADCIRC) tidal model (http://adcirc.org/), and river discharge from the United States Geological Survey (USGS). Surface fluxes derived from the WRF-ARW simulation mentioned above were calculated using the COARE bulk formulae [*Fairall et al.*, 2003]. The generic length scale k-kl vertical mixing scheme was used for water column turbulent mixing parameterization [*Umlauf and Burchard*, 2003; *Warner et al.*, 2005]. The Sandy hindcast simulation was initialized at 00:00 GMT on 25 October 2012 and run forward until 31 October 2012 07:00 GMT with hourly output. *Miles et al.* [2015] previously used this model configuration and setup to investigate sediment resuspension and transport processes during Sandy on the MAB.

Depth-average momentum balance terms were extracted from standard ROMS output and are represented by the following equations:
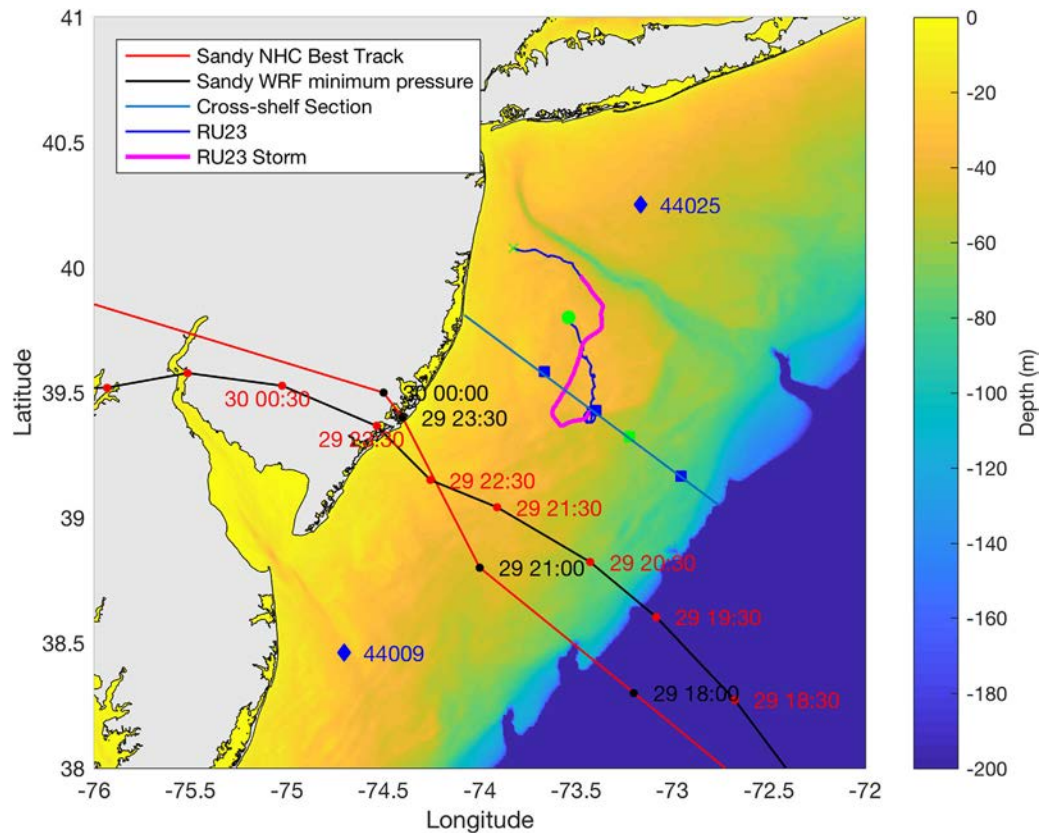
Figure 2. A zoomed in map of the New Jersey continental shelf and bathymetry with the NHC best track positions (red line) and times (dd HH:MM in black), and the WRF modeled track (black line) and times (dd HH:MM in red). The full glider RU23 track (blue) is plotted with the start location (green x) and recovery location (green circle) and the storm sampling period of 00:00 GMT on 28 October to 00:00 GMT on 31 October 2012 (magenta). NDBC buoys 44025 and 44009 are plotted with blue diamonds. The cross-shelf section used for Figures 7–12 is plotted in blue and the points for data extraction used in Figure 11 are plotted as blue squares. The third farthest extraction point from land at the 60 m isobath (green square) is used for Figure 6.

$$\underbrace{\frac{\partial u}{\partial t}}_{acceleration} = \underbrace{-\frac{\partial(uu)}{\partial x} - \frac{\partial(vu)}{\partial y}}_{horizontal\ advection} - \underbrace{\frac{1}{\rho_o}\frac{\partial P}{\partial x}}_{pressure\ gradient} + \left(\underbrace{\frac{\tau_s^x}{h\rho_o}}_{\substack{surface\\stress}} - \underbrace{\frac{\tau_b^x}{h\rho_o}}_{\substack{bottom\\stress}} \right) + \underbrace{fv}_{Coriolis} \tag{2}$$

$$\underbrace{\frac{\partial v}{\partial t}}_{acceleration} = \underbrace{-\frac{\partial(uv)}{\partial x} - \frac{\partial(vv)}{\partial y}}_{horizontal\ advection} - \underbrace{\frac{1}{\rho_o}\frac{\partial P}{\partial y}}_{pressure\ gradient} + \left(\underbrace{\frac{\tau_b^x}{h\rho_o}}_{\substack{surface\\stress}} - \underbrace{\frac{\tau_b^y}{h\rho_o}}_{\substack{bottom\\stress}} \right) - \underbrace{fu}_{Coriolis} \tag{3}$$

where t is time u and v are depth-averaged velocity in the x and y direction rotated into along-shelf and cross-shelf, P is pressure, ρ_o is a reference density of 1025 kg m^{-3}, τ_s^x and τ_s^y are wind stress, τ_b^x and τ_b^y are bottom stress, f is the Coriolis frequency. The horizontal viscosity terms were small in both the along and cross-shelf directions and were not included in equation (2) or (3). The temperature change rate equation was used to investigate the relative impact of mixing and advection on thermal changes throughout the water column as Sandy crossed the MAB shelf. Direct output from ROMS was used and is represented by:

$$\frac{\partial T}{\partial t} = -\frac{\partial(uT)}{\partial x} - \frac{\partial(vT)}{\partial y} - \frac{\partial(wT)}{\partial z} + \frac{\partial A_{kt}\frac{\partial T}{\partial z}}{\partial z} + D_T + F_T \tag{4}$$
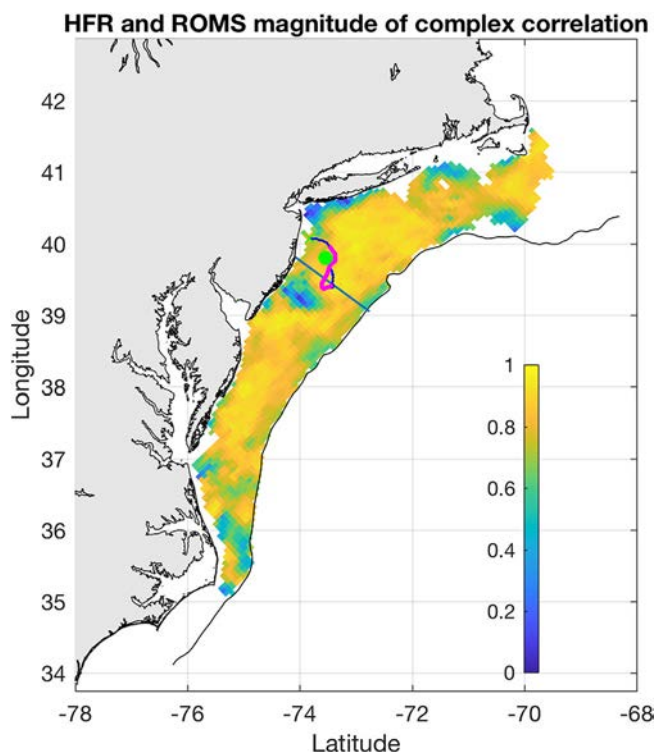
with surface and bottom boundary conditions of:

Figure 3. A map of the magnitude of the complex correlation between HF Radar hourly center-averaged surface currents and ROMS surface currents after interpolation to the nearest HF Radar grid point within the 150 m isobath (black contour). Correlation coefficients were made from model initialization at 00:00 GMT on 25 October to 00:00 GMT on 29 October 2012. The cross-shelf section used for Figures 7–12 is plotted in blue. The full glider RU23 track (blue) is plotted with the start location (green x) and recovery location (green circle) and the storm sampling period of 00:00 GMT on 28 October to 00:00 GMT on 31 October 2012 (magenta)

$$\left(A_{kt}\frac{\partial T}{\partial z}\right)_{z=0} = \frac{Q_{net}}{\rho_o C_P} \tag{5}$$

$$\left(A_{kt}\frac{\partial T}{\partial z}\right)_{z=-h} = 0 \tag{6}$$

where, variables are as above in (2) and (3) in addition to T as temperature, D_T as the horizontal diffusion term, F_T is friction, A_{kt} is the vertical eddy diffusivity, h is depth, Q_{net} is the surface net heat flux, and C_p is the specific heat capacity of seawater as 3985 J $(kg\ C)^{-1}$.

The ROMS-ESPreSSO model output has been extensively validated and performed well compared to numerous other regional models [*Wilkin and Hunter*, 2013]. A portion of the results section is dedicated to comparisons between the model output and water column glider data at a single location. Here we also include additional verification using hourly averaged HF Radar output starting at model initialization time of 00:00 GMT on 25 October to 00:00 GMT 29 October 2012 prior to station loss as Sandy made landfall. For this comparison, complex correlation coefficients were calculated between hourly 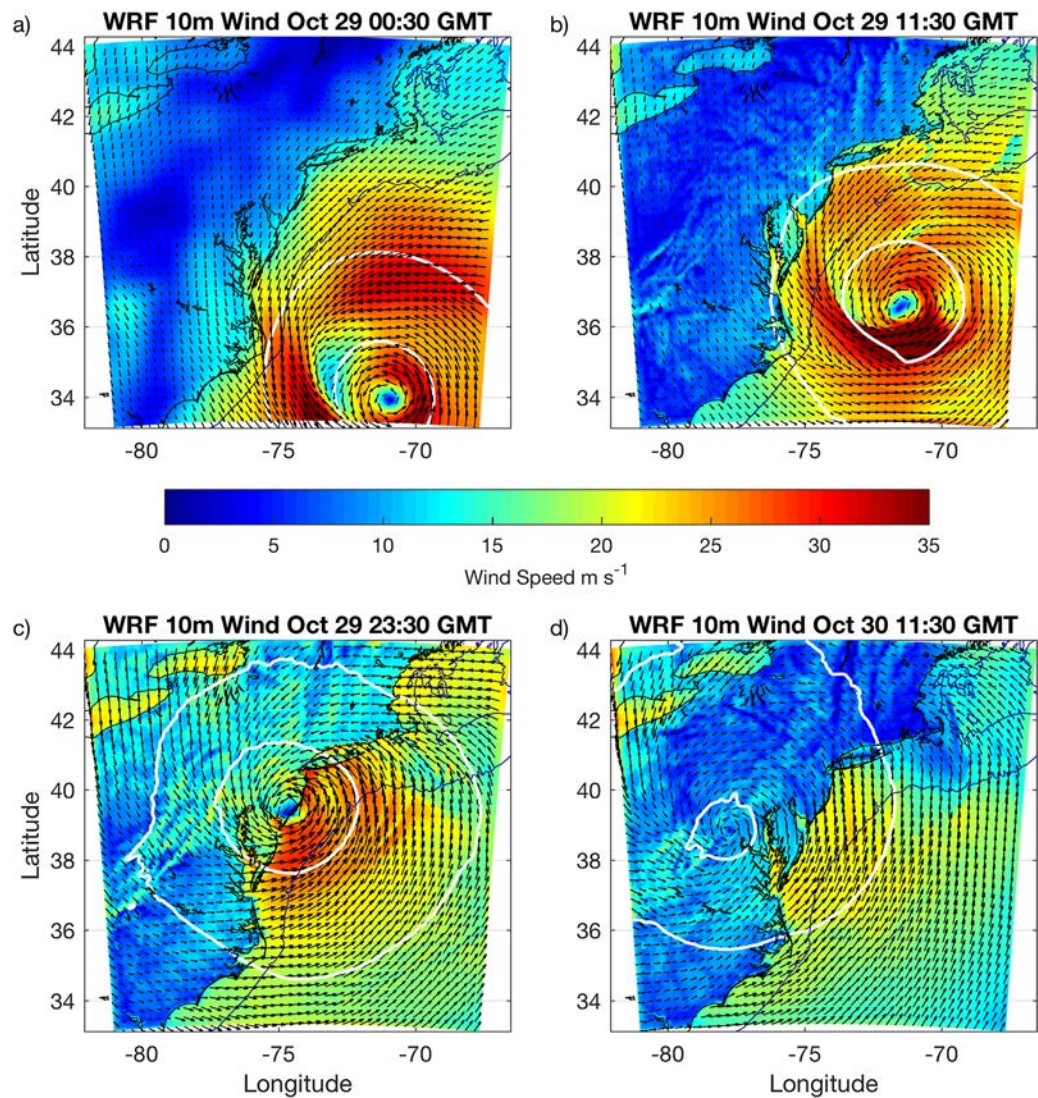time series of each ROMS-ESPreSSO grid point and nearest HF Radar grid point on the continental shelf (onshore of the 150 m isobath). Complex correlation coefficients showed that the ROMS model simulated surface currents well throughout the majority of the domain (Figure 3) while HF Radar data were available. In particular, the ROMS model simulated surface currents well in the vicinity of the deployed glider and cross-shelf transect used for analysis in Figures 7–12.

3. Results

3.1. Storm Conditions

NHC best track estimates show Hurricane Sandy moved along the southeastern coast of the United States on 26 October 2012 in a relatively weak state with a minimum pressure of 970 m bar and maximum sustained wind speeds of 35 m s^{-1} (Figure 1). Sandy moved parallel to the US East Coast through the 27th and 28th with pressure gradually falling and maximum sustained wind speeds staying near 35 m s^{-1}. Just before midnight on 28 October and into the 29, wind speeds began to increase rapidly and Sandy began to make a northwestward turn toward the MAB. Wind speeds continued to increase, reaching a peak over 40 m s^{-1} at approximately 12:00 GMT on 29 October and a minimum pressure of 940 mbar a few hours later. Maximum sustained wind speeds decreased back to 35 m s^{-1} just before landfall in southern NJ at 23:30 GMT on 29 October Sandy's eye entered the WRF model domain (Figure 4) on 29 October just after midnight GMT. Modeled 10 m winds were directed alongshore toward the southwest along the MAB coastline at over 20 m s^{-1}. Winds continued in the alongshore direction toward the southwest on the NJ shelf until landfall, while in the southern MAB winds were directed offshore toward the south and southeast. At landfall in southern NJ winds rapidly shifted offshore over Delaware, alongshore toward the northeast on the NJ continental shelf, and onshore toward Long Island, NY farther north. As Sandy crossed the MAB

Figure 4. Maps of the WRF 10 m wind speed (colors) and direction (arrows) with the 990 (outer white contour) and 970 (inner white contour) millibar surface pressures at (a) 00:30 GMT, (b) 11:30 GMT, (c) 23:30 GMT on 29 October, and 11:30 GMT on 30 October.

continental shelf (Figure 2) it made its closest approach to the south of glider RU23 at 21:00 GMT on 29 October while also passing between the two NOAA NDBC buoys 44025 to the north and 44009 to the south.

3.2. Glider Water Column Observations

Glider RU23 was deployed on 25 October just south of the Hudson Shelf Valley off the northern NJ coastline (Figure 2). It was piloted offshore out to the 40 m isobath prior to the storm in order to avoid being forced by strong currents into the coastline. During the storm forcing period the glider was pushed toward the southwest over 60 km. Regardless of this alongshore advection the glider stayed near the 40 m isobaths, and on the northern side of the storm track. With the shelf-wide scale of storm forcing we interpret RU23 glider output as a time series of vertical profiles (Figure 5), though alongshore variability in water column properties may exist. These time series show four distinct time periods. The initial stratified period between 00:00 and 12:00 GMT on 28 October showed warm surface temperatures of over 17°C in the upper 30 m and 10°C temperatures below the thermocline, uniform to the bottom. Glider mounted Aquadopp derived cross-shelf currents were mostly vertically uniform and reflected the barotropic tide, with a slight bottom intensification in the offshore direction. Along-shelf flow was vertically uniform and southwestward at near
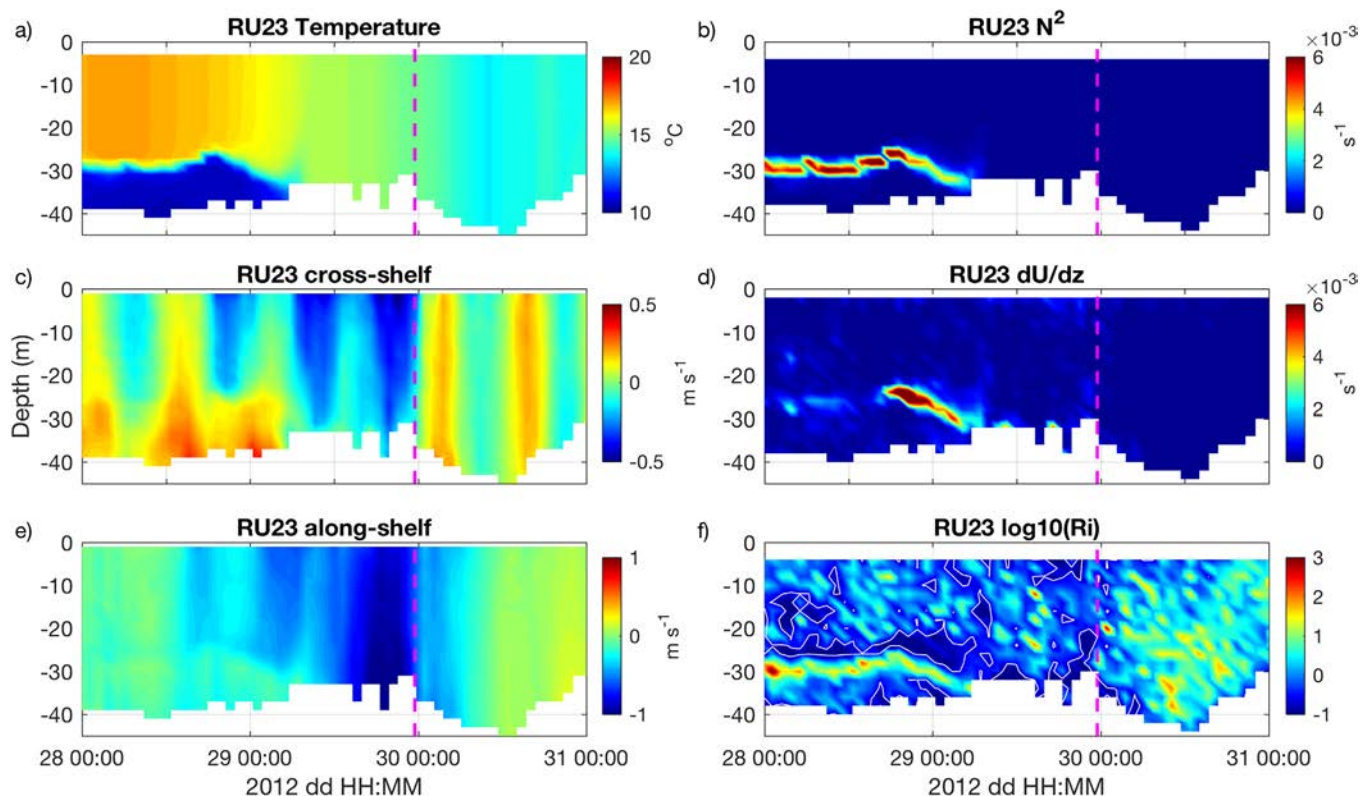
Figure 5. RU23 glider time series of vertical profiles extracted during the storm forcing period (track on magenta line shown in Figure 2). The vertical magenta line indicates Sandy landfall time. Variables plotted include (a) temperature, (c) cross-shelf velocity, (e) along-shelf velocity, (b) buoyancy frequency, (d) vertical shear of the horizontal velocity, and (f) the log10 of the Richardson number with Richardson number of 0.25 plotted with white contours. Velocity color bars are different in Figures 5c and 5e to highlight larger along-shelf magnitudes.

0.1 m s^{-1}. The sharp thermal stratification ($>5°$C m^{-1}) resulted in a stable pycnocline and large buoyancy frequencies. There was little vertical shear and the Richardson numbers remained large at the thermocline.

During the second time period between 12:00 GMT on 28 October and 06:00 GMT on the 29, the thermocline initially rose and then deepened dramatically, reaching the bottom in 12 h. Along-shelf currents increased to nearly 0.5 m s^{-1} in the surface layer and remained low in the bottom layer similar to during the initial stratified period. In the cross-shelf direction currents were onshore in the surface over 0.2 m s^{-1} while in the lower layer currents were offshore and near 0.4 m s^{-1} at 00:00 GMT on 29 October. While the thermocline deepened, vertical shear increased significantly, yet Richardson numbers remained above 0.25, indicating stable stratification was maintained up until the system transitioned from a two-layer to one-layer system by 06:00 GMT. During these 12 h the glider was advected ~12 km southward and remained on the northern side of the storm track, which indicates that much of the observed variability was temporal rather than spatial.

Between 06:00 GMT on 29 October and landfall at 23:30 GMT the water column responded to wind stress as a single layer. As the two-layer to one-layer transition occurred, the full water column cooled to just over 15°C, cross-shelf and along-shelf currents became relatively vertically uniform with primarily onshore flow with peak values near 0.2 m s^{-1}. Along-shelf flow was directed toward the southwest and reached near 1 m s^{-1} in the direction of the wind forcing. With a vertically well-mixed water column and uniform flow both buoyancy frequency and vertical shear were low and gradient Richardson numbers were variable throughout the water column. Following landfall storm-driven cross-shelf currents rapidly slowed and reflected the barotropic tide, while along-shelf currents slowed rapidly.

3.3. Hydrodynamic Model Output
ROMS output was extracted from a single location at the 60 m isobath (Figure 2) for comparison to glider cross sections (Figure 6). The model did not adequately represent the Cold Pool at the 40 m isobath where the glider was piloted but rather had a more defined Cold Pool farther offshore near the 60 m isobath.
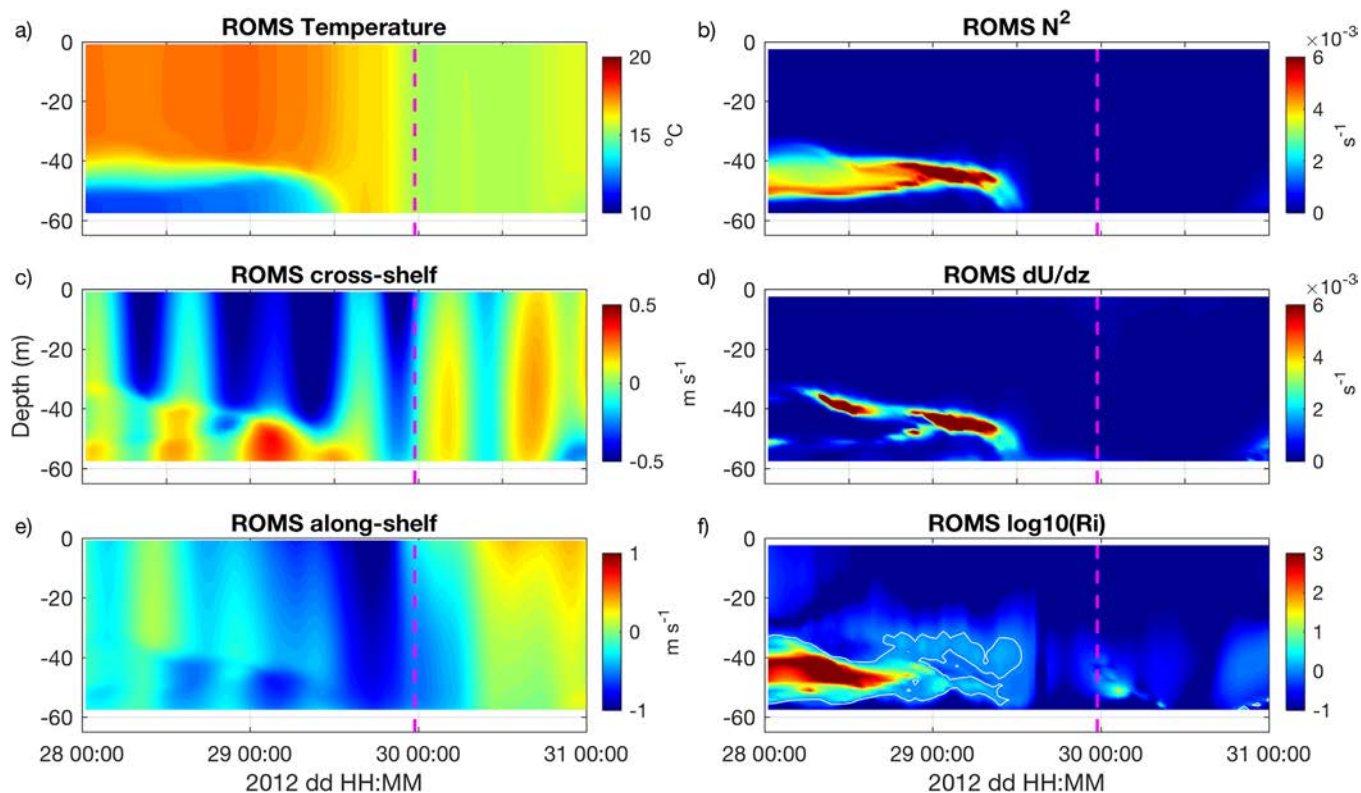
Figure 6. ROMS time series of vertical profiles extracted during the storm forcing period (green square plotted at the 60 m isobath shown in Figure 2). The vertical magenta line indicates Sandy landfall time. Variables plotted include (a) temperature, (c) cross-shelf velocity, (e) along-shelf velocity, (b) buoyancy frequency, (d) vertical shear of the horizontal velocity, and (f) the $\log_{10}$ of the Richardson number with Richardson number of 0.25 plotted with white contours. Velocity color bars are different in Figures 6c and 6e to highlight larger along-shelf magnitudes.

During the initial stratified period from 00:00 GMT and 12:00 GMT on 28 October modeled surface temperatures were only slightly warmer than observations, near 18°C while bottom temperatures were warmer than observations at 11.5°C with a total difference of 6.5°C compared to 7°C observed by the glider. Currents were similar to glider sampled velocities with bottom intensified offshore flow in the cross-shelf direction and weak and variable along-shelf flow. At this farther offshore location stratification persisted until 12:00 GMT on 29 October, 6 h later than at the glider location. While the surface and bottom temperatures were similar to observations the thermocline was much thicker and weaker with a vertical temperature gradient of ~0.3°C m^{-1} resulting in lower buoyancy frequencies than those observed by the glider over a broader vertical area, yet Richardson numbers remained above 0.25 throughout the storm forcing period. As stratification persisted longer in the model at this location flow was two-layer during the main storm forcing period with strong onshore flow near 0.5 m s^{-1} in the surface layer and offshore flow near 0.2 m s^{-1} near the bottom. Along-shelf southwestward flow did not reach its peak until after stratification eroded at 12:00 GMT on 29 October. While the thermocline deepened, N^2 remained elevated despite increasing vertical shear and, while Richardson numbers in the thermocline were reduced, they continued to remain above 0.25 until the system transitioned from two-layers to one. Despite differences between the glider observations and model output the observed water column features and transition from a two-layers to one-layer circulation are well represented.

Cross-shelf sections of the model simulated temperature and velocity were extracted along the transect shown in Figure 2 for three times, 12:30 GMT on 28 October, 00:30 GMT on 29 October, and 12:30 GMT on 29 October (Figure 7). At 12:30 GMT on 28 October a thin-layer of partially mixed Cold Pool water was present inshore up to the 20 m isobath with core Cold Pool water extending over a thicker bottom layer out to the shelf-break. Cross-shelf currents were directed offshore within the bottom Cold Pool layer and onshore in the surface layer. Along-shelf velocities were low throughout the water column at this time. Vertical velocities show downwelling at the inshore edge of the Cold Pool and over the deep ocean with upwelling
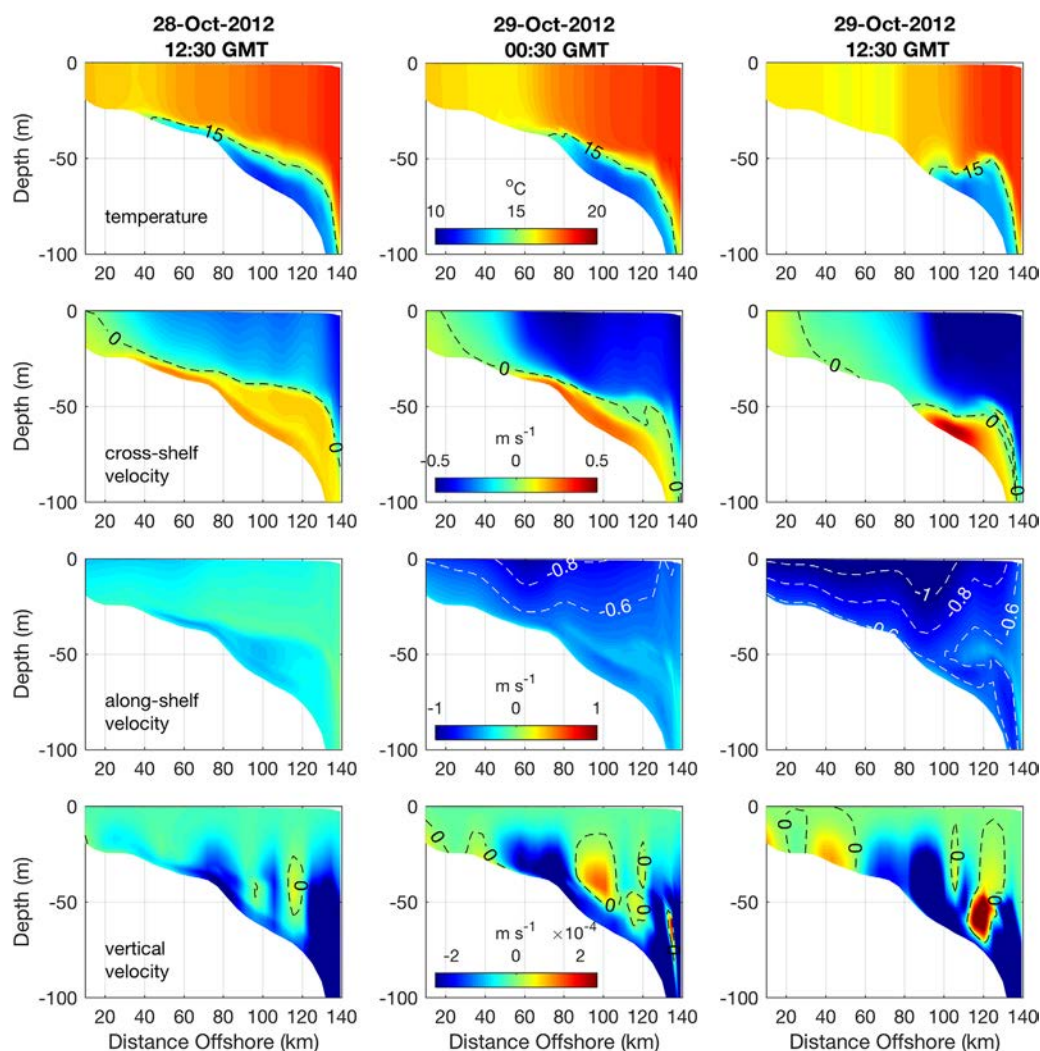
Figure 7. Cross-shelf sections of temperature (row 1), cross-shelf velocity (row 2), along-shelf velocity (row 3), and vertical velocity (row 4) extracted from the cross-shelf section shown in Figure 2. Times extracted include 12:30 GMT on 28 October, 00:30 GMT on 29 October, and 12:30 GMT on 29 October. Contours are used to show the approximate Cold Pool extent (row 1), to provide 0 crossing reference for velocities in rows 2 and 4, and to highlight the along-shelf southwestward velocities of 1, 0.8, and 0.6 m s^{-1} (row 3). Velocity color bars are different in rows 2–4.

within the core Cold Pool offshore. Over the next 24 h, a clear frontal region developed with vertically uniform temperatures that expanded across the innershelf. Cross-shelf velocities were onshore in the surface layer over the stratified region and slowed as they approached the unstratified innershelf. Bottom intensified offshore flow was evident within the Cold Pool and downwelling offshore flow occurred throughout the entire Cold Pool. Over the innershelf along-shelf velocities were toward the southwest throughout the entire water column, and were enhanced in an along-shelf jet toward the southwest at the downwelling front just above the innershelf edge of the Cold Pool at 12:30 GMT on 29 October.

Hovmöller diagrams of temperature and velocity were plotted along the same cross-shelf section to continuously track the temporal evolution of the surface and bottom layers (Figure 8). At 00:00 GMT on the 28th surface (Figure 8a) and bottom (Figure 8b) temperatures are similar out to 25 km offshore representing the well-mixed region inshore of the Cold Pool shown in Figure 7. The inshore edge of the Cold Poolis hereafter referred to as the Cold Pool Front and is defined by the cross-shelf temperature gradient in the bottom layer. The Cold Pool extended across the shelf between approximately 40 km and over 130 km offshore. Over the next 48 h until landfall the Cold Pool Front moved offshore by over 70 km. Within the innershelf bottom temperatures remained near 16°C throughout the duration of the storm while surface temperatures
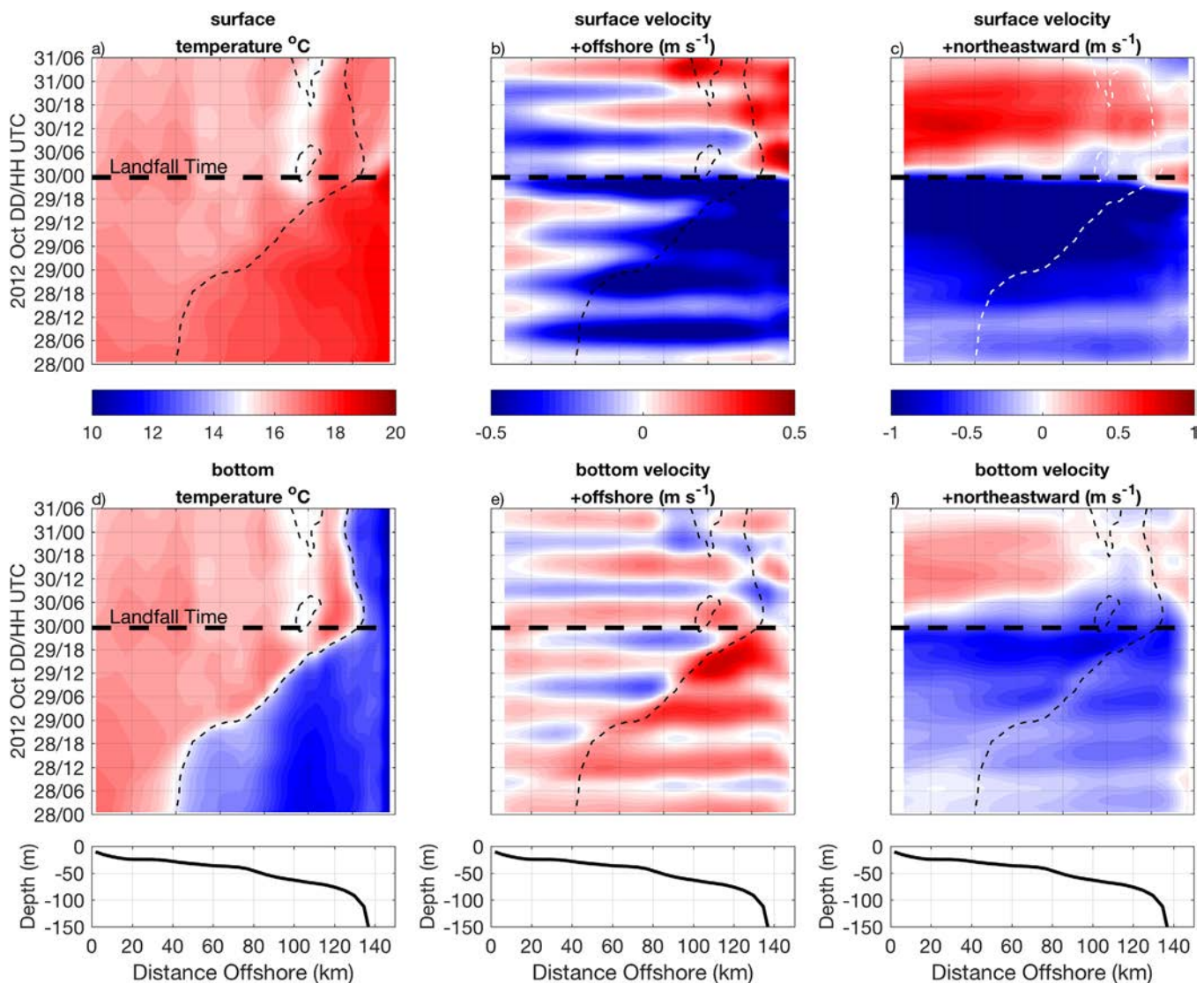
Figure 8. Hovmöller diagrams of hourly ROMS output extracted from the cross-shelf section shown in Figure 2. Extracted variables include (a) surface temperature, (b) surface cross-shelf velocity, (c) surface along-shelf velocity, (d) bottom temperature, (e) bottom cross-shelf velocity, and (f) bottom along-shelf velocity. Cross-shelf and along-shelf velocities are positive in the offshore and northeastward directions. Black dashed contours represent the 15°C bottom temperature or the approximate position of the Cold Pool Front. Horizontal dashed lines represent Sandy's landfall time. The bottom three plots are the bathymetry and distance offshore extracted from the cross-shelf line.

cooled by approximately 1°C out to 100 km offshore on the landward side of the Cold Pool Front. Enhanced cooling (warming) of the surface (bottom) occurred at landfall time 100 km offshore down (up) to 14.5°C. Landward of the Cold PoolFront, cross-shelf surface velocities were directed offshore. Seaward of the Cold Pool Front surface currents were directed onshore indicating a surface convergence zone and downwelling at the Cold Pool Front consistent with Figure 7. In the bottom layer, cross-shelf currents landward of the Cold Pool front were weak and directed onshore, while cross-shelf currents seaward of the Cold Pool front were strong and directed offshore indicating a region of divergence and offshore Cold Pool advection. Along-shelf currents during the ahead-of-eye period were consistently in the southwestward direction and were $\sim$1 m s^{-1} in the surface layer. Along-shelf bottom currents were in the same direction as surface currents but weaker until the main storm forcing period between 06:00 GMT on 29 October and just after landfall at 03:00 GMT on 30 October.

To further investigate the processes responsible for the observed and simulated coastal ocean response to Sandy, a time series of depth-averaged momentum balance terms are shown in Figures 9 and 10, with each term defined in equation (2) and (3) for cross-shelf and along-shelf directions respectively. The horizontal
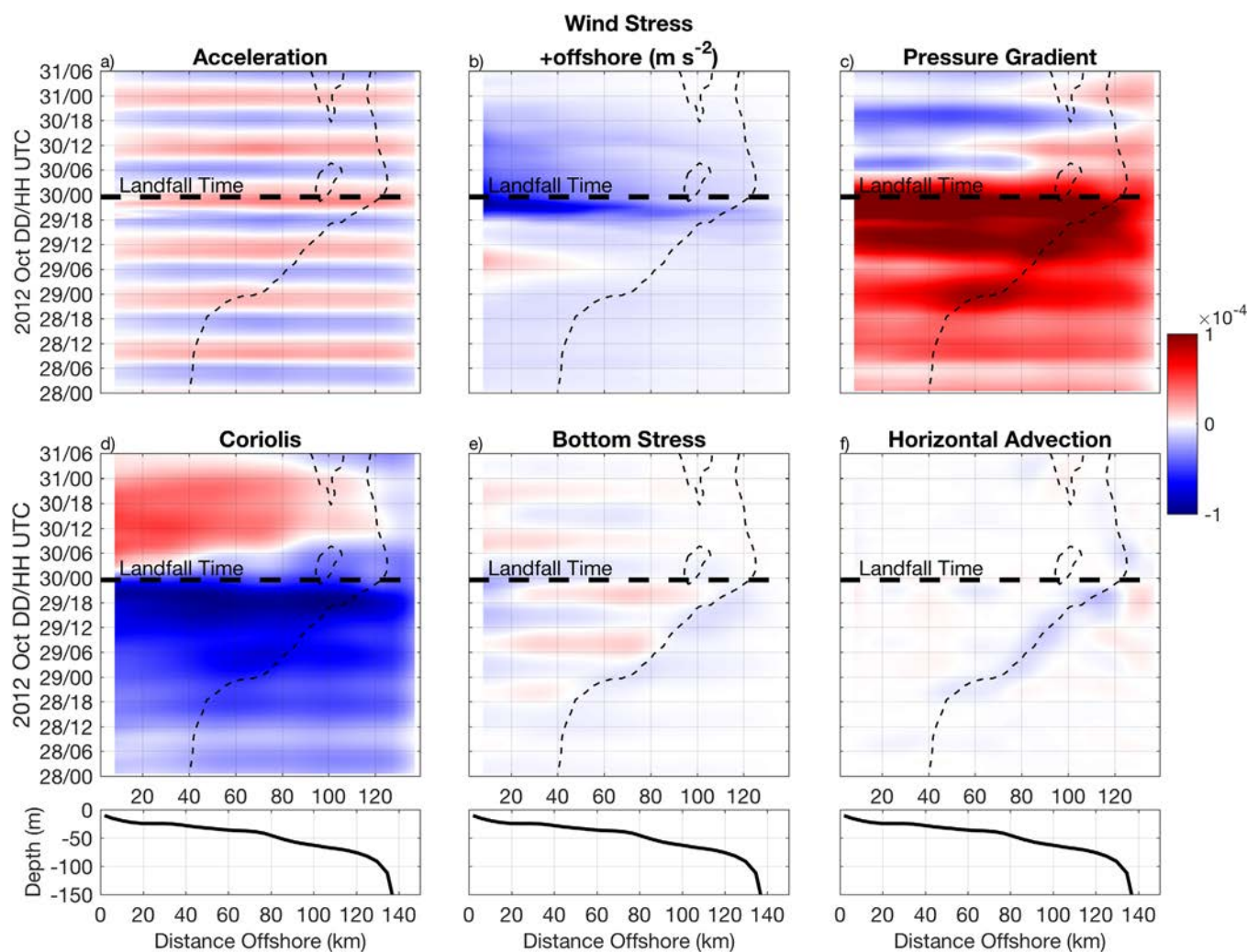
Figure 9. Hovmöller diagrams of hourly ROMS output of the depth-averaged cross-shelf momentum balance terms (equation (2)) extracted from the cross-shelf section shown in Figure 2. Extracted variables include (a) acceleration, (b) wind stress, (c) pressure gradient, (d) Coriolis, (e) bottom stress, and (f) horizontal advection. Positive is in the offshore directions Black dashed contours represent the 15°C bottom temperature or the approximate position of the Cold Pool Front. Horizontal dashed lines represent Sandy's landfall time. The bottom three plots are the bathymetry and distance offshore extracted from the cross-shelf line.

viscosity term was negligible and was not included. In both the cross-shelf and along-shelf directions the acceleration is tidally dominated with enhanced northeastward acceleration as Sandy made landfall. Wind stress was consistent with observed wind fields (Figure 4) alongshore toward the southwest and slightly offshore prior to landfall and rotated to northeastward and slightly onshore after landfall. The pressure gradient term was one of the dominant cross-shelf terms prior to landfall and was positive indicating an offshore directed sea-surface slope, or sea-surface setup along the coastline. This cross-shelf pressure gradient was balanced by a negative Coriolis term prior to landfall indicating that the coastal ocean over much of the shelf was nearly in geostrophic balance prior to Sandy making landfall. On the landward side of the Cold Pool Front, where the water column was vertically uniform, bottom stress was large and northeastward ahead of landfall, opposing the southwestward bottom currents. Depth-averaged horizontal advection terms in both the cross-shelf and along-shelf directions were small.

To quantitatively assess the impact of mixing and advection on the destratification of the continental shelf water column, we plotted time series profiles (Figure 11) of the temperature rate of change, combined temperature horizontal and vertical advection, and temperature vertical diffusion terms from equation (4). Data were extracted from four points on the cross-shelf transect shown in Figure 2 representing the approximate 20, 40, 60, and 80 m isobaths with the 60 m point aligning with the data extracted from ROMS in Figure 6. Tidal influences can be seen at all four locations in the total temperature rate and advection terms,
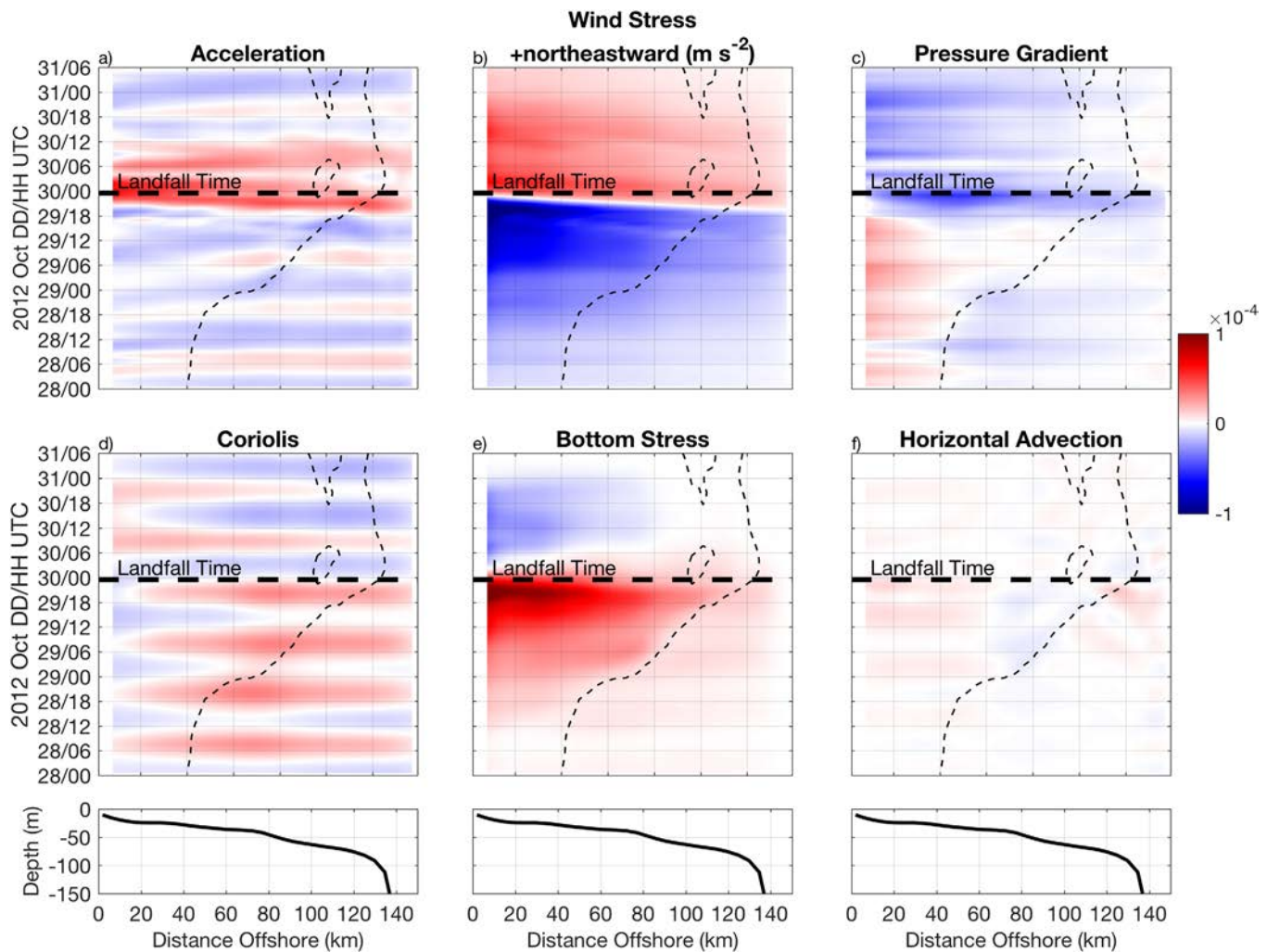
Figure 10. Hovmöller diagrams of hourly ROMS output of the depth-averaged along-shelf momentum balance terms (equation (3)) extracted from the cross-shelf section shown in Figure 2. Extracted variables include (a) acceleration, (b) wind stress, (c) pressure gradient, (d) Coriolis, (e) bottom stress, and (f) horizontal advection. Positive is in the southwestward direction. Black dashed contours represent the 15°C bottom temperature or the approximate position of the Cold Pool Front. Horizontal dashed lines represent Sandy's landfall time. The bottom three plots are the bathymetry and distance offshore extracted from the cross-shelf line.

particularly in the surface layer but not in vertical diffusion terms. While these tidal features are ubiquitous they are small relative to the large storm-driven advective terms and only represent changes on the order of 0.1°C at each given location. Aside from the tidally driven advection the inner shelf point exhibits little change throughout the storm forcing period and no vertical diffusion of temperature as temperature is vertically uniform. At the 40 m isobath cooling is evident at 00:00 GMT on the 29th in the surface layer and warming near the bottom. Cooling in the surface layer was driven by vertical diffusion of Cold Pool water while warming near the bottom was a combination of both advection and vertical diffusion. At the 60 m isobath a similar and more obvious pattern is evident with cooling in the surface layer and warming and deepening of the bottom layer between 00:00 GMT and landfall at 23:30 GMT on 29 October. Negative vertical diffusion of temperature is evident throughout the surface layer while positive vertical diffusion is only evident at the top of Cold Pool waters indicating erosion of the top of the Cold Pool into the surface layer. Within the Cold Pool, temperature advection was positive and dominated the temperature rate of change indicating that Cold Pool water was exported consistent with offshore flow observed in the near bottom layer in Figures 5 (glider time series), 6 (model time series), 7 model cross-shelf section), and 8 (model Hovmöller). At the offshore location there is a distinct periodic warming and cooling at the top of the Cold Pool by temperature advection, potentially linked with internal wave dynamics, though the period of the signal is unclear due to the short duration of the response. A distinct positive advective signal was again evident
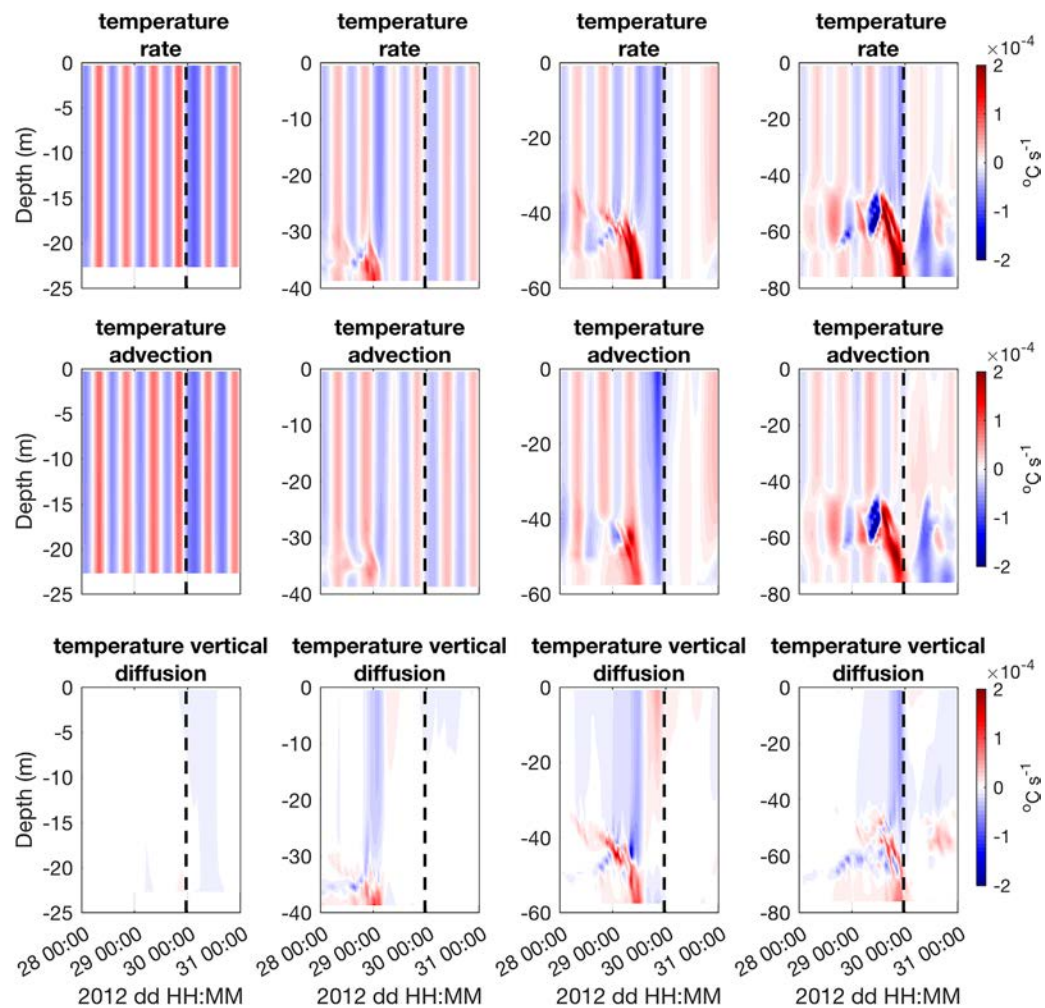
Figure 11. Time series of vertical profiles of the temperature diagnostic terms (equation (4)) extracted from the 4 cross-shelf points shown in Figure 2. Variables include the temperature rate of change (row 1), combined horizontal and vertical advection terms (row 2), and temperature vertical diffusion terms (row 3). The dashed vertical black line is Sandy's landfall time at 23:30 GMT on 29 October 2012.

near bottom at, and just after, landfall consistent with offshore advection of the Cold Pool seen at the shallower 60 m location. Vertical diffusion of temperature is limited and irregular pre-landfall while cooling is seen in the sea-surface after landfall when winds and currents reverse direction.

4. Discussion

The observed and modeled offshore bottom velocities, stable water column, momentum balance terms, and temperature diagnostics indicate that mixing processes alone were not sufficient for the seaward progression of the Cold Pool Front ∼70 km offshore ahead of Sandy's landfall in New Jersey. The observed ahead-of-eye-center surface cooling was similar to previous studies of tropical cyclones that impacted the MAB during the stratified season such as Irene [*Glenn et al.*, 2016; *Seroka et al.*, 2016] and Barry [*Seroka*, 2017]. However, unlike these previous storms Sandy induced an extreme coastal ocean response to a tropical cyclone with the offshore advection of the Cold Pool Front. Three features of Sandy contributed to this coastal ocean response. (1) Sandy's cross-shelf track: typically tropical cyclones enter the stratified MAB from the south and travel alongshore toward the northeast [*Hall and Yonekura*, 2013] leading to initially onshore leading edge winds that rotate into alongshore southward or northward as a storm passes depending on its inshore or offshore track. Synthetic tropical cyclones that followed a similar cross-shelf track to Sandy was found to have a return rate of greater than 700 years for the MAB region [*Hall and Sobel*, 2013], and only five storms of tropical storm strength or greater have crossed nearly perpendicular to the NJ shelf

since 1889 (https://coast.noaa.gov/hurricanes/). (2) Sandy was an exceptionally large storm: After exiting the Caribbean and passing the Bahamas, Sandy's radius of maximum winds increased to over 185 km, a large size it maintained until landfall [*Blake et al.*, 2013]. This large size is nearly 4 times the average radius of maximum wind for typical U.S. landfalling storms [*Hsu and Yan*, 1998]. 3) Sandy was a slow moving storm: Typical storms within the MAB region have translation speeds of approximately 40 km h^{-1} [*Landsea et al.*, 2015], while Sandy had an average translation speed between 00:00 GMT on 28 October to 23:30 GMT on 29 October of 27 km h^{-1} [*Blake et al.*, 2013].

The above three factors combined to produce a prolonged exposure of the stratified coastal ocean to alongshore southwestward downwelling favorable wind stress for nearly 48 h, or over 2.5 inertial periods, which are approximately 18 hours on the central MAB. The idealized two-dimensional downwelling response of a stratified coastal ocean to alongshore wind stress has been described for the Oregon [*Allen and Newberger*, 1996] and Mid Atlantic [*Austin and Lentz*, 2002] continental shelves. In *Austin and Lentz* [2002], they used an idealized version of the Princeton Ocean Model to represent a gently sloping continental shelf with a highly stratified water column typical of the Northeastern U.S. in summer. Downwelling favorable winds of $\sim$8 m s^{-1} were ramped up over one inertial period and held constant for nearly 2 weeks. They simulated onshore Ekman transport in the surface that deepened the pycnocline in the nearshore region until it intersected the bottom and was advected offshore. In their simulation they found that over the first inertial period alongshore wind stress resulted in onshore Ekman transport in the surface layer and led to a barotropic response that advected the bottom downwelling front seaward. For two-dimensional cross-shelf circulation they assumed that the vertically integrated transport was zero and could be divided into the surface Ekman transport, the barotropic interior, and the bottom Ekman transport. In the initial forcing period when the bottom Ekman layer is not spun up the cross-shelf balance is between the surface Ekman transport and the barotropic interior flow [*Dever*, 1997]. From *Austin and Lentz* [2002], the offshore displacement of the front for the barotropic response scaled with:

$$x_{baro}(t) = \sqrt{\int_0^t \frac{2U^s}{\alpha}dt + X_0^2} \tag{7}$$

where x_{baro} is the cross-shelf displacement, t is time, α is the slope of the shelf, X_0 is the initial front position, and U^s is the surface Ekman transport such that $U^s = \tau/\rho f$ where τ is the alongshore wind stress, ρ is a reference density, and f is the Coriolis frequency. The limited along-shelf bottom stress, elevated along-shelf wind stress, and elevated cross-shelf pressure gradient components of the momentum balance (Figure 9 and 10) during the first inertial period starting at 00:00 GMT on 28 October 2012 support this. In *Austin and Lentz* [2002], after the first inertial period the bottom Ekman layer develops and the bottom Ekman transport approximately equals the surface Ekman transport and the offshore displacement of the front scaled with:

$$x_{ek}(t) = X_0 + \sqrt{\int_0^t \frac{2U^s}{\alpha}dt} \tag{8}$$

which is also supported by the increased along-shelf bottom stress matching the along-shelf wind stress at 06:00 GMT on 29 October 2012 (Figure 10).

To determine if the Cold Pool Front displacement in Sandy fits with the theoretical scaling in *Austin and Lentz* [2002] we used constants of $\alpha = 0.00055$, $X_0 = 40$ km, $f = 10^{-4}$ s^{-1}, $\rho = 1025$ kg m^{-3}. The alongshore wind stress from WRF was averaged along the cross-shelf section in Figure 2 hourly. The winds between 00:00 to 18:00 GMT 28 October were used with equation (7) and during the remaining time period until landfall 18:00 GMT on 28 October to 23:30 GMT on 29 October with equation (8). The frontal displacement from concatenating the results from equations (7) and (8) is shown in Figure 12 along with the offshore displacement of the 15°C isotherm which was previously shown in Figures 8–10 to represent the Cold Pool Front. The 15°C isotherm position and estimated frontal displacement were in good agreement with a barotropic displacement of $\sim$10 km in the first inertial period and an Ekman driven offshore displacement of $\sim$60 km in the remaining 1.5 inertial periods until landfall at the top of Figure 12. Key assumptions necessary for the *Austin and Lentz* [2002] scaling to be valid include (1) that conservation of mass is a strong constraint on the flow, (2) along-shelf variability in the flow is small compared to the cross-shelf variability, or
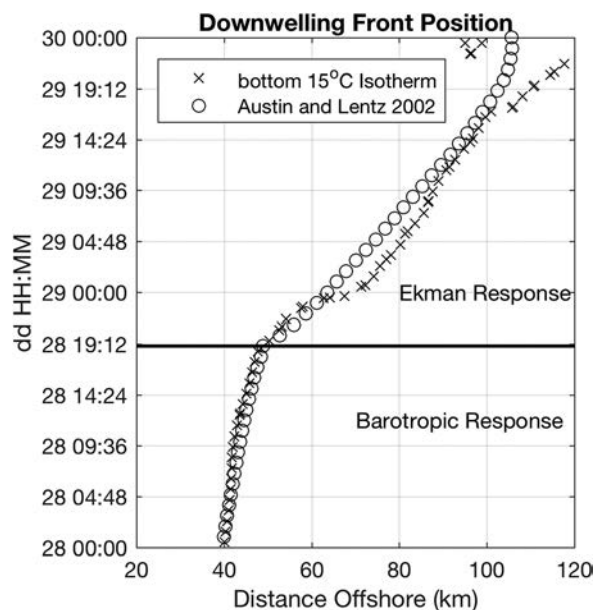
Figure 12. A Hovmöller diagram showing the offshore position of the 15°C bottom contour (x's) extracted from the ROMS model to represent the approximate position of the Cold Pool Front, and the position estimated from [*Austin and Lentz*, 2002] using the barotropic response (Equation 7) for the first inertial period and the Ekman response (equation (8)) for the remainder of Sandy's storm forcing period (o's). The solid horizontal line indicates the end of the first inertial period.

that the flow is approximately two-dimensional, (3) Ekman transport in the surface layer is well established and independent of turbulent closure schemes; and (4) deepening of the mixed-layer is limited.

This coastal ocean response to a tropical cyclone in the stratified MAB is unique to Hurricane Sandy. Alongshore winds measured at buoy 44025 (Figure 2) for Sandy showed that winds steadily increased from 5 to over 20 m s^{-1} and persisted for over 48 h ahead of landfall. An analysis of along-shelf wind speed from buoy 44025 from 1985 to present, which included the 11 storms that impacted the MAB during the stratified season highlighted in *Glenn et al.* [2016] show that no tropical cyclones resulted in alongshore wind stress that exceeded 18 h, thus none were capable of inducing the offshore Ekman response observed on the shelf during Sandy. While cross-shelf tracking storms are not typical over the MAB, NOAA storm track maps (coast.noaa.gov/hurricanes) show the southeastern coast of China and the Yellow Sea, regions with highly stratified water columns in summer [*Chen et al.*, 1994; *Li et al.*, 2012], are frequently impacted by cross-shelf tracking storms that may induce significant alongshore wind stress prior to landfall. A sediment resuspension and transport study on Typhoon Morakot in 2009 [*Li et al.*, 2012] shows seaward displacement of cold bottom waters offshore. While not explicitly tested, the offshore advection of the Cold Pool ahead-of-eye-center may have been a contributing factor to the limited deintensification observed in Hurricane Sandy and more research on the coastal ocean response to tropical cyclones is needed.

In addition to the impacts on the water column structure, the observed and modeled offshore advection of the downwelling front ahead-of-eye-center also had implications for sediment resuspension and transport. Sandy had a large impact on coastal sediment resuspension and transport throughout the MAB [*Trembanis et al.*, 2013; *Miles et al.*, 2015; *Warner et al.*, 2017]. The 70 km cross-shelf advection of the Cold Pool reduced water column stability on the innershelf and allowed for significant sediment resuspension and transport. On the offshore side of the downwelling front, where the water column was stratified, bottom stress was limited and subsequently sediment resuspension and transport along with cross-shelf currents was limited. On the inshore side of the downwelling front bottom stress was enhanced, sediment was resuspended throughout the full water column, and along-shelf flow transported sediment from the northern portion of the NJ Shelf near the Hudson Shelf Valley to the southern portion of the NJ Shelf near Delaware bay [*Miles et al.*, 2015]. This rapid resuspension and resorting of shelf sediments in a few hours, which was on the scale of trawling and dredging impacts, has potential implications for benthic habitats [*Fanning et al.*, 1982; *Thrush and Dayton*, 2002] and for prediction of the fate and effects of pollutants introduced at the coastline [*Biscaye et al.*, 1988]. In addition to changes in sediment character, downwelling circulation on the NJ shelf has previously also been found to redistribute surfclam larvae across the shelf and may have implications for their settlement and recruitment among other macrofaunal communities [*Grassle et al.*, 2006]. Also, rapid temperature changes with the passage of a warm downwelling front may have negative physiological impacts on benthic organisms [*Thiyagarajan et al.*, 2000].

5. Conclusions

In this study we use an integrated ocean observing system that consists of an HF Radar network, Teledyne-Webb Slocum gliders, buoys, and regional ocean and atmospheric modeling to detail the coastal ocean

response to Hurricane Sandy. Many studies have detailed the impact of tropical cyclones on the upper ocean, particularly while these storms transit over the deep sea [*Price*, 1981; *Price et al.*, 1994; *Zedler et al.*, 2002; *D'Asaro*, 2003; *Jaimes and Shay*, 2009; *Jaimes et al.*, 2011; *Sanford et al.*, 2011]. While many of these studies have focused on shear-driven vertical mixing, a study by *Yablonsky and Ginis* [2009] showed that modeling three-dimensional upwelling processes is necessary to accurately represent sea surface cooling induced by tropical cyclones over the deep ocean. More recent studies [*Glenn et al.*, 2016; *Seroka et al.* 2017; *Seroka et al.*, 2016] have shown three-dimensional coastal ocean processes can contribute to rapid sea-surface cooling through enhanced vertical shear ahead-of-eye center. This paper adds to that growing knowledge by detailing an additional case-study where ahead-of-eye-center downwelling circulation can advect the Cold Pool offshore and reduce stratification on the shallow inner shelf before eye-passage. While to-date this is a unique process observed during hurricane Sandy there is evidence that oceanographic conditions and storm tracks off of Southeastern China may result in similar dynamics. The results of this study continue to highlight the need for combined ocean observing systems and regional modeling in order to further understand the range of coastal ocean responses to tropical cyclones and potential feedbacks on storm intensity.

References

Allen, J. S., and P. A. Newberger (1996), Downwelling circulation on the Oregon continental shelf. Part I: Response to idealized forcing, *J. Phys. Oceanogr.*, 26(10), 2011–2035, doi:10.1175/1520-0485(1996)026 < 2011:DCOTOC>2.0.CO;2.

Austin, J., and S. Lentz (2002), The inner shelf response to wind-driven upwelling and downwelling., *J. Phys. Oceanogr.*, 32, 2171–2193.

Avila, L. A., and J. P. Cangialosi (2012), Tropical Cyclone Report: Hurricane Irene, National Hurricane Center Tropical Cyclone Rep. AL092011, 45 pp. [Available online at http://www.nhc.noaa.gov/data/tcr/AL092011_Irene.pdf.]

Barrick, D. E. (1971a), Theory of HF and VHF propagation across the rough sea. 1: The effective surface impedance for a slightly rough highly conducting medium at grazing incidence, *Radio Sci.*, 6(5), 517–526, doi:10.1029/RS006i005p00517.

Barrick, D. E. (1971b), Theory of HF and VHF propagation across the rough sea. 2: Application to HF and VHF propagation above the sea, *Radio Sci.*, 6(5), 527–533, doi:10.1029/RS006i005p00527.

Bender, M., and I. Ginis (2000), Real-case simulations of hurricane-ocean interaction using a high-resolution coupled Model: Effects on hurricane intensity, *Mon. Weather Rev.*, 128, 917–946.

Biscaye, P. E., R. F. Anderson, and B. L. Deck (1988), Fluxes of particles and constituents to the eastern United States continental slope and rise: SEEP—I, *Cont. Shelf Res.*, 8(5–7), 855–904

Black, P. G., E. A. D'Asaro, T. B. Sanford, W. M. Drennan, J. A. Zhang, J. R. French, P. P. Niiler, E. J. Terrill, and E. J. Walsh (2007), Air-sea exchange in hurricanes: Synthesis of observations from the coupled boundary layer air-sea transfer experiment, *Bull. Am. Meteorol. Soc.*, 88(3), 357–374, doi:10.1175/BAMS-88-3-357.

Blake, E. S., T. B. Kimberlain, R. J. Berg, P. C. John, and J. L. Beven II (2013), Tropical cyclone report: Hurricane sandy, *Natl. Hurric. Cent.*, 12, 1–157.

Briscoe, M. G., D. L. Martin, and T. C. Malone (2008), Evolution of regional efforts in international GOOS and US IOOS, *Mar. Technol. Soc. J.*, 42(3), 4–9.

Cahill, B., O. Schofield, R. Chant, J. Wilkin, E. Hunter, S. Glenn, and P. Bissett (2008), Dynamics of turbid buoyant plumes and the feedbacks on near-shore biogeochemistry and physics, *Geophys. Res. Lett.*, 35, L10605, doi:10.1029/2008GL033595.

Cangialosi, J. P., and J. L. Franklin (2016), National Hurricane Center Forecast VErification Report: 2015 Hurricane Season, Miami, Fla.

Castelao, R., S. Glenn, O. Schofield, R. Chant, J. Wilkin, and J. Kohut (2008), Seasonal evolution of hydrographic fields in the central Middle Atlantic Bight from glider observations, *Geophys. Res. Lett.*, 35, L03617, doi:10.1029/2007GL032335.

Chen, C., R. C. Beardsley, R. Limeburner, and K. Kim (1994), Comparison of winter and summer hydrographic observations in the Yellow and East China Seas and adjacent Kuroshio during 1986, *Cont. Shelf Res.*, 14(7–8), 909–929, doi:10.1016/0278-4343(94)90079-5.

Chen, S. S., J. F. Price, W. Zhao, M. A. Donelan, and E. J. Walsh (2007), The CBLAST-Hurricane program and the next-generation fully coupled atmosphere-wave-ocean models for hurricane research and prediction, *Bull. Am. Meteorol. Soc.*, 88(3), 311–317, doi:10.1175/BAMS-88-3-311.

Considine, T. J., C. Jablonowski, B. Posner, and C. H. Bishop (2004), The value of hurricane forecasts to oil and gas producers in the Gulf of Mexico, *J. Appl. Meteorol.*, 43, 1270–1282.

Cornillon, P., L. Stramma, and J. F. Price (1987), Satellite measurements of sea surface cooling during hurricane Gloria, *Nature*, 326(6111), 373–375, doi:10.1038/326373a0.

D'Asaro, E. A. E. (2003), The ocean boundary layer below hurricane dennis, *J. Phys. Oceanogr.*, 33(3), 561–579, doi:10.1175/1520-0485(2003)033 < 0561:TOBLBH>2.0.CO;2.

Davis, R., C. Eriksen, and C. Jones (2002), Autonomous buoyancy-driven underwater gliders, in *Technology and Applications of Autonomous Underwater Vehicles*, edited by G. Griffiths, pp. 37–58, Taylor and Francis, London.

DeMaria, M., C. R. Sampson, J. A. Knaff, and K. D. Musgrave (2014), Is tropical cyclone intensity guidance improving?, *Bull. Am. Meteorol. Soc.*, 95(3), 387–398, doi:10.1175/BAMS-D-12-00240.1.

Dever, E. P. (1997), Wind-forced cross-shelf circulation on the Northern California shelf, *J. Phys. Oceanogr.*, 27(8), 1566–1580, doi:10.1175/1520-0485(1997)027 < 1566:WFCSCO>2.0.CO;2.

Domingues, R., G. Goni, F. Bringas, S.-K. Lee, H.-S. Kim, G. Halliwell, J. Dong, J. Morell, and L. Pomales (2015), Upper ocean response to Hurricane Gonzalo (2014): Salinity effects revealed by targeted and sustained underwater glider observations, *Geophys. Res. Lett.*, 42, 7131–7138, doi:10.1002/2015GL065378.

du Plessis, M., S. Swart, I. J. Ansorge, and A. Mahadevan (2017), Submesoscale processes accelerate seasonal restratification in the Subantarctic Ocean, *J. Geophys. Res. Oceans*, 122, 2960–2975, doi:10.1002/2016JC012494.

Emanuel, K. (2016), Will global warming make hurricane forecasting more difficult?, *Bull. Am. Meteorol. Soc.*, 98(3), 495–501, doi:10.1175/BAMS-D-16-0134.1.

Emanuel, K., C. DesAutels, C. Holloway, and R. Korty (2004), Environmental control of tropical cyclone intensity, *J. Atmos. Sci.*, *61*(7), 843–858, doi:10.1175/1520-0469(2004)061 < 0843:ECOTCI>2.0.CO;2.

Emanuel, K. A. (1999), Thermodynamic control of hurricane intensity, *Nature*, *401*(6754), 665–669.

Fairall, C. W., E. F. Bradley, J. E. Hare, A. A. Grachev, and J. B. Edson (2003), Bulk parameterization of air-sea fluxes: Updates and verification for the COARE algorithm, *J. Clim.*, *16*(4), 571–591.

Fanning, K. A., K. L. Carder, and P. R. Betzer (1982), Sediment resuspension by coastal waters: A potential mechanism for nutrient re-cycling on the ocean's margins, *Deep Sea Res., Part A*, *29*(8), 953–965, doi:10.1016/0198-0149(82)90020-6.

Fisher, E. L. (1958), Hurricanes and the sea-surface temperature field, *J. Meteorol.*, *15*(3), 328–333, doi:10.1175/1520-0469(1958)015 < 0328: HATSST>2.0.CO;2.

Fritz, H. M., C. D. Blount, S. Thwin, M. K. Thu, and N. Chan (2009), Cyclone Nargis storm surge in Myanmar, *Nat. Geosci.*, *2*(7), 448–449, doi: 10.1038/ngeo558.

Garau, B., S. Ruiz, W. G. Zhang, A. Pascual, E. Heslop, J. Kerfoot, and J. Tintoré (2011), Thermal lag correction on slocum CTD glider data, *J. Atmos. Oceanic Technol.*, *28*(9), 1065–1071, doi:10.1175/JTECH-D-10-05030.1.

Georgas, N., P. Orton, A. Blumberg, L. Cohen, D. Zarrilli, and L. Yin (2014), The impact of tidal phase on hurricane Sandy's flooding around New York City and Long Island Sound, *J. Extrem. Events*, *1*(1), Article 1450006, doi:10.1142/S2345737614500067.

Glenn, S., C. Jones, M. Twardowski, L. Bowers, J. Kerfoot, D. Webb, and O. Schofield (2008), Glider observations of sediment resus-pension in a Middle Atlantic Bight fall transition storm, *Limnol. Oceanogr. Methods*, *53*(5 part 2), 2180–2196, doi:10.4319/lo.2008.53.5_part_2.2180.

Glenn, S. M., T. N. Miles, G. N. Seroka, Y. Xu, R. K. Forney, F. Yu, H. Roarty, O. Schofield, and J. Kohut (2016), Stratified coastal ocean interac-tions with tropical cyclones, *Nat. Commun.*, *7*, Article 10887, 1–10, doi:10.1038/ncomms10887.

Grassle, J. P., H. Ma, and R. J. Chant (2006), Vertical distribution of bivalve larvae along a cross-shelf transect during summer upwelling and downwelling, *Mar. Biol.*, *149*(5), 1123–1138, doi:10.1007/s00227-006-0287-3.

Haidvogel, D. B., et al. (2008), Ocean forecasting in terrain-following coordinates: Formulation and skill assessment of the Regional Ocean Modeling System, *J. Comput. Phys.*, *227*(7), 3595–3624, doi:10.1016/j.jcp.2007.06.016.

Hall, T., and E. Yonekura (2013), North American tropical cyclone landfall and SST: A statistical model study, *J. Clim.*, *26*(21), 8422–8439, doi:10.1175/JCLI-D-12-00756.1.

Hall, T. M., and A. H. Sobel (2013), On the impact angle of Hurricane Sandy's New Jersey landfall, *Geophys. Res. Lett.*, *40*, 2312–2315, doi:10.1002/grl.50395.

Hidaka, K., and Y. Akiba (1955), Upwelling induced by a circular wind system, *Rec. Ocean. Work. Jpn.*, *2*, 7–18.

Hofmann, E., J.-N. Druon, K. Fennel, M. Friedrichs, D. Haidvogel, C. Lee, A. Mannino, C. McClain, R. Najjar, and J. O'Reilly (2008), Eastern US continental shelf carbon budget integrating models, data assimilation, and analysis, *Oceanography*, *21*(1), 86–104.

Houghton, R. W., R. Schlitz, R. C. Beardsley, B. Butman, and J. L. Chamberlin (1982), The Middle Atlantic bight cold pool: Evolution of the temperature structure during summer 1979, *J. Phys. Oceanogr.*, *12*(10), 1019–1029, doi:10.1175/1520-0485.

Hsu, S. A., and Z. Yan (1998), A note on the radius of maximum wind for hurricanes, *J. Coast. Res.*, *14*(2), 667–668.

Jaimes, B., and L. K. Shay (2009), Mixed layer cooling in mesoscale oceanic eddies during hurricanes Katrina and Rita, *Mon. Weather Rev.*, *137*(12), 4188–4207, doi:10.1175/2009MWR2849.1.

Jaimes, B., and L. K. Shay (2015), Enthalpy and momentum fluxes during hurricane earl relative to underlying ocean features, *Mon. Weather Rev.*, *143*(1), 111–131, doi:10.1175/MWR-D-13-00277.1.

Jaimes, B., L. K. Shay, and G. R. Halliwell (2011), The response of quasigeostrophic oceanic vortices to tropical cyclone forcing, *J. Phys. Oce-anogr.*, *41*(10), 1965–1985, doi:10.1175/JPO-D-11-06.1.

Kohut, J., H. Roarty, E. Randall-Goodwin, S. Glenn, and C. S. Lichtenwalner (2012), Evaluation of two algorithms for a network of coastal HF radars in the Mid-Atlantic Bight, *Ocean Dyn.*, *62*(6), 953–968, doi:10.1007/s10236-012-0533-9.

Kohut, J. T., S. M. Glenn, and J. D. Paduan (2006), Inner shelf response to Tropical Storm Floyd, *J. Geophys. Res.*, *111*, C09S91, doi:10.1029/2003JC002173.

Kossin, J. P., K. A. Emanuel, and G. A. Vecchi (2014), The poleward migration of the location of tropical cyclone maximum intensity, *Nature*, *509*(7500), 349–352.

Landsea, C. W., J. L. Franklin, and J. L. Beven (2015), The revised Atlantic hurricane database (HURDAT2), Sponsor National Oceanographic and Atmospheric Administration, National Hurricane Center. [Available at http://www.nhc.noaa.gov/data/hurdat/hurdat2-format-atlan-tic.pdf.]

Leipper, D. F. (1967), Observed ocean conditions and hurricane Hilda, 1964, *J. Atmos. Sci.*, *24*(2), 182–186, doi:10.1175/1520-0469(1967)024 < 0182:OOCAHH>2.0.CO;2.

Lentz, S. (2003), Evolution of stratification over the New England shelf during the Coastal Mixing and Optics study, August 1996–June 1997, *J. Geophys. Res.*, *108*(C1), 3008, doi:10.1029/2001JC001121.

Lentz, S. J. (2017), Seasonal warming of the Middle Atlantic Bight Cold Pool, *J. Geophys. Res. Oceans*, *122*, 941–954, doi:10.1002/2016JC012201.

Li, Y., A. Wang, L. Qiao, J. Fang, and J. Chen (2012), The impact of typhoon Morakot on the modern sedimentary environment of the mud deposition center off the Zhejiang-Fujian coast, China, *Cont. Shelf Res.*, *37*, 92–100, doi:10.1016/j.csr.2012.02.020.

Miles, T., S. Glenn, and O. Schofield (2013), Temporal and spatial variability in fall storm induced sediment resuspension on the Mid-Atlantic Bight, *Cont. Shelf Res.*, *63*, S36–S49.

Miles, T., G. Seroka, J. Kohut, O. Schofield, and S. Glenn (2015), Glider observations and modeling of sediment transport in Hurricane Sandy, *J. Geophys. Res. Oceans*, *120*, 1771–1791, doi:10.1002/2014JC010474.

Miller, K. G., P. J. Sugarman, J. V. Browning, B. P. Horton, A. Stanley, A. Kahn, J. Uptegrove, and M. Aucott (2009), Sea-level rise in New Jersey over the past 5000 years: Implications to anthropogenic changes, *Global Planet. Change*, *66*(1–2), 10–18, doi:10.1016/j.gloplacha.2008.03.008.

Moore, A. M., H. G. Arango, G. Broquet, B. S. Powell, A. T. Weaver, and J. Zavala-Garay (2011), The Regional Ocean Modeling System (ROMS) 4-dimensional variational data assimilation systems, *Prog. Oceanogr.*, *91*(1), 34–49, doi:10.1016/j.pocean.2011.05.004.

Nicholson, S.-A., M. Lévy, J. Llort, S. Swart, and P. M. S. Monteiro (2016), Investigation into the impact of storms on sustaining summer pri-mary productivity in the Sub-Antarctic Ocean, *Geophys. Res. Lett.*, *43*, 9192–9199, doi:10.1002/2016GL069973.

Price, J. F. (1981), Upper Ocean Response to a Hurricane, *J. Phys. Oceanogr.*, *11*(2), 153–175, doi:10.1175/1520-0485(1981)011 < 0153:UOR-TAH>2.0.CO;2.

Price, J. F., T. B. Sanford, and G. Z. Forristall (1994), Forced stage response to a moving hurricane, *J. Phys. Oceanogr.*, *24*(2), 233–260, doi:10.1175/1520-0485(1994)024 < 0233:FSRTAM>2.0.CO;2.

Roarty, H., et al. (2010), Operation and application of a regional high-frequency radar network in the Mid-Atlantic Bight, *Mar. Technol. Soc. J.*, *44*(6), 133–145.

Ruiz, S., L. Renault, B. Garau, and J. Tintoré (2012), Underwater glider observations and modeling of an abrupt mixing event in the upper ocean, *Geophys. Res. Lett.*, *39*, L01603, doi:10.1029/2011GL050078.

Sanford, T. B., J. F. Price, and J. B. Girton (2011), Upper-ocean response to hurricane Frances (2004) observed by profiling EM-APEX Floats, *J. Phys. Oceanogr.*, *41*(6), 1041–1056, doi:10.1175/2010JPO4313.1.

Seroka, G. (2016), Stratified coastal ocean interactions with hurricanes and the sea breeze in the U.S. Mid-Atlantic.

Seroka, G., T. Miles, Y. Xu, J. Kohut, O. Schofield, and S. Glenn (2016), Hurricane Irene sensitivity to stratified coastal ocean cooling, *Mon. Weather Rev.*, *144*(9), 3507–3530, doi:10.1175/MWR-D-15-0452.1.

Seroka, G., T. Miles, Y. Xu, J. Kohut, O. Schofield, and S. Glenn (2017), Rapid shelf-wide cooling response of a stratified coastal ocean to hurricanes, *J. Geophys. Res. Ocean.*, doi:10.1002/2017JC012756.

Shchepetkin, A. F., and J. C. McWilliams (2005), The regional oceanic modeling system (ROMS): A split-explicit, free-surface, topography-following-coordinate oceanic model, *Ocean Modell.*, *9*(4), 347–404, doi:10.1016/j.ocemod.2004.08.002.

Shchepetkin, A. F., and J. McWilliams (2009a), Computational kernel algorithms for fine-scale, multi-process, long-time oceanic simulations, *Handbook Numer. Anal.*, *14*(8), 121–183, doi:10.1016/S1570-8659(08)01202-0.

Shchepetkin, A. F., and J. C. McWilliams (2009b), Correction and commentary for "Ocean forecasting in terrain-following coordinates: Formulation and skill assessment of the regional ocean modeling system" by Haidvogel et al., J. Comp. Phys. 227, pp. 3595–3624, *J. Comput. Phys.*, *228*(24), 8985–9000, doi:10.1016/j.jcp.2009.09.002.

Skamarock, W., J. Klemp, J. Dudhia, D. O. Gill, D. M. Barker, M. G. Duda, X.-Y. Huang, W. Wang, and J. G. Powers (2008), A description of the advanced research WRF version 3, NCAR Tech. Note NCAR/TN−475+STR, 475 pp., Natl. Cent. for Atmos. Res., Boulder, Colo.

Stramma, L., P. Cornillon, and J. Price (1986), Satellite observations of sea surface cooling by hurricanes, *J. Geophys. Res.*, *91*, 5031–5035.

Swart, S., S. J. Thomalla, and P. M. S. Monteiro (2015), The seasonal cycle of mixed layer dynamics and phytoplankton biomass in the Sub-Antarctic Zone: A high-resolution glider experiment, *J. Mar. Syst.*, *147*, 103–115, doi:10.1016/j.jmarsys.2014.06.002.

Teague, C. C. (1971), *High Frequency Resonant Scattering Techniques for the Observation of Directional Ocean Wave Spectra*, Dep. of Electr. Eng., Stanford Univ., Stanford, Calif.

Thiyagarajan, V., Y. Nancharaiah, V. Venugopalan, K. V. Nair, and T. Subramoniam (2000), Relative tolerance of cirripede larval stages to acute thermal shock: A laboratory study, *J. Therm. Biol.*, *25*(6), 451–457, doi:10.1016/S0306-4565(00)00010-3.

Thrush, S. F., and P. K. Dayton (2002), Disturbance to marine benthic habitats by trawling and dredging: Implications for marine biodiversity, *Annu. Rev. Ecol. Syst.*, *33*(1), 449–473, doi:10.1146/annurev.ecolsys.33.010802.150515.

Todd, R. E., D. L. Rudnick, M. R. Mazloff, R. E. Davis, and B. D. Cornuelle (2011a), Poleward flows in the southern California Current System: Glider observations and numerical simulation, *J. Geophys. Res.*, *116*, C02026, doi:10.1029/2010JC006536.

Todd, R. E., D. L. Rudnick, R. E. Davis, and M. D. Ohman (2011b), Underwater gliders reveal rapid arrival of El Niño effects off California's coast, *Geophys. Res. Lett.*, *38*, L03609, doi:10.1029/2010GL046376.

Torn, R. D., and C. Snyder (2012), Uncertainty of tropical cyclone best-track information, *Weather Forecasting*, *27*(2006), 715–729, doi:10.1175/WAF-D-11-00085.1.

Trembanis, A., C. DuVal, J. Beaudoin, V. Schmidt, D. Miller, and L. Mayer (2013), A detailed seabed signature from Hurricane Sandy revealed in bedforms and scour, *Geochem. Geophys. Geosyst.*, *14*, 4334–4340, doi:10.1002/ggge.20260.

Umlauf, L., and H. Burchard (2003), A generic length-scale equation for geophysical turbulence models, *J. Mar. Res.*, *61*(2), 235–265.

Visbeck, M. (2002), Deep velocity profiling using lowered acoustic doppler current profilers: Bottom track and inverse solutions, *J. Atmos. Oceanic Technol.*, *19*, 794–807.

Wang, D., and H. Zhao (2008), Estimation of phytoplankton responses to Hurricane Gonu over the Arabian Sea based on ocean color data, *Sensors*, *8*(8), 4878–4893, doi:10.3390/s8084878.

Warner, J. C., C. R. Sherwood, H. G. Arango, and R. P. Signell (2005), Performance of four turbulence closure models implemented using a generic length scale method, *Ocean Modell.*, *8*(1–2), 81–113, doi:10.1016/j.ocemod.2003.12.003.

Warner, J. C., W. C. Schwab, J. H. List, I. Safak, M. Liste, and W. Baldwin (2017), Inner-shelf ocean dynamics and seafloor morphologic changes during Hurricane Sandy, *Cont. Shelf Res.*, *138*, 1–18, doi:10.1016/j.csr.2017.02.003.

Wilkin, J. L., and E. J. Hunter (2013), An assessment of the skill of real-time models of Mid-Atlantic Bight continental shelf circulation, *J. Geophys. Res. Oceans*, *118*, 2919–2933, doi:10.1002/jgrc.20223.

Xu, Y., B. Cahill, J. Wilkin, and O. Schofield (2013), Role of wind in regulating phytoplankton blooms on the Mid-Atlantic Bight, *Cont. Shelf Res.*, *63*(Mld), S26–S35, doi:10.1016/j.csr.2012.09.011.

Yablonsky, R. M., and I. Ginis (2008), Improving the ocean initialization of coupled hurricane-ocean models using feature-based data assimilation, *Mon. Weather Rev.*, *136*(7), 2592–2607, doi:10.1175/2007MWR2166.1.

Yablonsky, R. M., and I. Ginis (2009), Limitation of one-dimensional ocean models for coupled hurricane-ocean model forecasts, *Mon. Weather Rev.*, *137*(12), 4410–4419, doi:10.1175/2009MWR2863.1.

Zambon, J. B., R. He, and J. C. Warner (2014), Tropical to extratropical: Marine environmental changes associated with Superstorm Sandy prior to its landfall, *Geophys. Res. Lett.*, *41*, 8935–8943, doi:10.1002/2014GL061357.

Zedler, S. E., T. D. Dickey, S. C. Doney, J. F. Price, X. Yu, and G. L. Mellor (2002), Analyses and simulations of the upper ocean's response to Hurricane Felix at the Bermuda Testbed Mooring site: 13–23 August 1995, *J. Geophys. Res.*, *107*(C12), 3232, doi:10.1029/2001JC000969.

Zhang, W. G., J. L. Wilkin, and R. J. Chant (2009), Modeling the pathways and mean dynamics of river plume dispersal in the New York Bight, *J. Phys. Oceanogr.*, *39*(5), 1167–1183, doi:10.1175/2008JPO4082.1.